JBC RESEARCH ARTICLE

Functional inhibition of c-Myc using novel inhibitors identified through "hot spot" targeting

Received for publication, December 15, 2021, and in revised form, March 18, 2022 Published, Papers in Press, April 1, 2022,
https://doi.org/10.1016/j.jbc.2022.101898

Ashutosh Singh[1], Prateek Kumar[1], Sailu Sarvagalla[2], Taniya Bharadwaj[1], Namyashree Nayak[1], Mohane Selvaraj Coumar[3], Rajanish Giri[1], and Neha Garg[4,*]

From the [1]School of Basic Sciences, Indian Institute of Technology Mandi, Mandi, HP, India; [2]Division of Biology, Indian Institute of Science Education and Research (IISER)-Tirupati, Tirupati, AP, India; [3]Centre for Bioinformatics, School of Life Sciences, Pondicherry University, Kalapet, Puducherry, India; [4]Department of Medicinal Chemistry, Institute of Medical Sciences, Banaras Hindu University, Varanasi, UP, India

Edited by Karen Fleming

Protein–protein interactions drive various biological processes in healthy as well as disease states. The transcription factor c-Myc plays a crucial role in maintaining cellular homeostasis, and its deregulated expression is linked to various human cancers; therefore, it can be considered a viable target for cancer therapeutics. However, the structural heterogeneity of c-Myc due to its disordered nature poses a major challenge to drug discovery. In the present study, we used an *in silico* alanine scanning mutagenesis approach to identify "hot spot" residues within the c-Myc/Myc-associated factor X interface, which is highly disordered and has not yet been systematically analyzed for potential small molecule binding sites. We then used the information gained from this analysis to screen potential inhibitors using a conformation ensemble approach. The fluorescence-based biophysical experiments showed that the identified hit molecules displayed noncovalent interactions with these hot spot residues, and further cell-based experiments showed substantial *in vitro* potency against diverse c-Myc-expressing cancer/stem cells by deregulating c-Myc activity. These biophysical and computational studies demonstrated stable binding of the hit compounds with the disordered c-Myc protein. Collectively, our data indicated effective drug targeting of the disordered c-Myc protein *via* the determination of hot spot residues in the c-Myc/Myc-associated factor X heterodimer.

In normal cells, protein–protein interactions (PPIs) play a crucial role in normal cellular functioning *via* regulating various biological processes; one of many is the formation of specific and dynamic interaction in the cell signaling pathway (1–3). On an estimate, around 130,000 to 650,000 PPIs are present in the complex human interactome and responsible for numerous biological functions in normal and diseased cells (4, 5). The deregulated PPI is reported in various disease states, including cancer (6, 7). A perturbated PPI leads to altered behavior of a given metabolic pathway, making the PPI an attractive target for drug discovery. The knowledge of the PPI structural aspect indicates that the energy distribution is not uniform in a given PPI, and only a small subset of amino acids will have the majority of contribution in binding free energy than others (8, 9). These residues significantly contribute to binding free energy in PPIs are called "hot spots" (10). A more specific definition of a hot spot is an amino acid residue when mutated with alanine results in a decrease of at least 2.0 kcal/mol in the binding free energy (11, 12). Detection of these hot spots in deregulated PPIs has helped researchers for structure-based drug discovery.

c-Myc/Myc-associated factor X (MAX) is a classic example of PPI, which plays a crucial role in cellular homeostasis by regulating various cellular processes, like cell cycle progression, cell growth and division, metabolism, cell adhesion, mobility, telomerase activity, and apoptosis (13–15). The heterodimer controls the expression of nearly 15% of the entire human genome *via* binding to the palindromic enhancer box sequences or E-box present at the promoter of the target genes (16). The expression level and activity of c-Myc is highly controlled in the normal cells, and its deregulation is associated with various solid and hematological tumors showing aggressive nature and chemoresistance (17, 18). The involvement of c-Myc in various cancers makes it a promising therapeutic target for developing novel antineoplastic drugs. In the last 2 decades, researchers have employed various strategies to inhibit the functionality of c-Myc (19–21). These strategies include the transcriptional and post-translational targeting of c-Myc. Till now, various small molecules and peptide-based inhibitors have been reported, but they all fail in the clinical trials due to unappropriated pharmacokinetic behavior and lack of *in vivo* potency.

Targeting c-Myc/MAX heterodimerization has always been preferred to discover potent inhibitor that exclusively inhibits the regulatory functionality of c-Myc. However, several challenges are associated with therapeutic intervention against c-Myc that restrict the development of c-Myc-targeted antineoplastic drugs. The Myc/MAX interacting interface is relatively large (~3200 Å^2), flat, and lacks appropriate and uncharacterized binding sites for small molecule binding (22, 23). The c-Myc and MAX belong to the basic helix-loop-helix leucine-zipper (bHLH-LZ) protein family. The C-terminal region of c-Myc is a

* For correspondence: Neha Garg, nehagarg@bhu.ac.in.

bHLH-LZ domain, which binds with the partner protein MAX to form the oncogenic heterodimer. In isolation, the bHLH-LZ domain of c-Myc is highly disordered (partially folded), which undergoes ordered transformation after dimerization with MAX *via* adopting a stable helical conformation (24, 25). The dynamic nature of the bHLH-LZ domain of c-Myc provides it the binding plasticity to interact with various other partners, like MIZ1 and SKP2.

Intrinsically disordered proteins (IDPs) are poorly structured proteins with a highly flexible backbone giving rise to an undefined secondary or tertiary structure (26, 27). It is estimated that more than one-third of the entire human genome and more than 50% of transcription factors are disordered (28, 29). Increasing shreds of evidence have shown the implication of IDPs in disease, making them the critical target for therapeutic interventions (30–32). The traditional drug discovery approach targets the target protein's structured active site, leading to competitive or noncompetitive inhibition of the target. However, the IDPs behave as a "protein cloud" that lacks a structured active site and presents a conformational heterogeneity, thereby posing problems in the rational drug design (33). Overcoming these challenges, various approaches have been used to target an IDP *via* a small molecule (30). The first one targets different disordered ensembles by a small molecule, and the second approach employs the targeting of the partner protein where binding of the small molecule with the partner protein will inhibit binding with the partner IDP target. Targeting the conformational ensembles of IDPs has emerged as a credible strategy because the molecule that can bind to the dynamic structure may potentially inhibit the interaction with the partner proteins. However, this strategy is quite challenging and complicated as the traditional drug discovery approach cannot be employed because of the lack of a well-characterized target structure.

The interacting interface of c-Myc and MAX is relatively large, and all the residues shaping in this interface do not contribute equally to the binding free energy of c-Myc/MAX interaction. The critical amino acid residues, also called hot spots, exhibiting significant contribution in c-Myc and MAX interaction has not yet been previously characterized. Therefore, in the present study, we first identified the hot spot residues of this oncogenic dimer using the computational alanine scanning mutagenesis (ASM). The ASM is a powerful *in silico* approach that has been widely used to accurately identify the hot spot residues in a PPI *via* sequentially mutating the interface residues to alanine and calculating the change in binding free energy. The identified hot spots were then used to discover new inhibitor molecules *via* targeting the disordered c-Myc using the conformation ensemble approach. The screened molecules showed excellent binding with the disordered c-Myc, thereby inhibiting its regulatory functionality leading to apoptotic cell death of c-Myc expressing cancer and cancer stem cells (CSCs).

Results

Identification of hot spots in c-Myc/MAX interaction

To identify the hot spot residues in the c-Myc/MAX PPI complex, we have carried out molecular dynamic (MD) simulation for 40 ns using the simulated annealing with NMR-derived energy restraints (SANDER) and particle mesh Ewald molecular dynamics module of Amber software suit. The MD simulation trajectory snapshots were saved for every 200 ps and were analyzed using the CPPTRAJ module of Amber. The protein stability was evaluated based on its root mean square deviation (RMSD) from its initial coordinates. The evaluated protein backbone RMSD revealed that initially it raised to 5.5 Å for a period of 20 ns due to conformational changes in the terminal region of the c-Myc/MAX complex. Then, the protein backbone RMSD decreased to 3.5 Å and maintained stability throughout the simulation without much fluctuation (Fig. 1*A*).

After MD simulation, the final 10% of the trajectory snapshots (last 4 ns frames) were used to calculate the binding free energy of the protein complex using the molecular mechanics Poisson–Boltzmann surface area (MM-PBSA) method and was found to be −115.85 kcal/mol (Table S3). Next, the per-residue energy decomposition was carried out to know the residue-wise energy contribution for the native protein–protein complex formation. The results revealed that the residues Leu917, Leu924, Gln927, Leu943, Ile950, Val953, Leu960, Leu967, Arg971, Leu974, and Leu978 of c-Myc were contributing more than −2.0 kcal/mol, whereas the remaining residues contributed less than −2.0 kcal/mol (Fig. 1*B* and Table S4). Following the per-residue energy contribution analysis, ASM was carried out to know the binding energy difference between the native and mutant protein complex. For this purpose, the residues of c-Myc in the interface region were mutated one by one to alanine, and the change in the binding-free energy between the native and the mutant complex was calculated (Fig. 1*C* and Table S4). Next, the residues were classified as hot spots ($\Delta\Delta G > 4.0$ kcal/mol; Leu924, Gln927, Leu943, Ile950, Glu957, Arg971, and Leu974), warm spots ($\Delta\Delta G$ = 2.0–4.0 kcal/mol; Leu917, Phe921, Val953, Gln954, Glu956, Leu960, Glu964, Leu967, and Leu978), and null spots ($\Delta\Delta G < 2.0$ kcal/mol; Glu916, Ser920, Asp926, Val941, Thr947, Glu963, and Lys977). The identified hot spot and warm spot residues of c-Myc are shown in Figure 1*D*. The identified hot spot and warm spot information was further used to screen the library of molecules with the potential to inhibit the functionality of c-Myc.

Structural dynamics of c-Myc through all-atom MD simulations

Before examining the structural dynamics of c-Myc using MD simulation, seven well-known online disorder predictors were employed to examine the disorderness of the c-Myc's bHLH-LZ region. According to our analysis, the predicted percentage of intrinsic disorder is calculated to be 50%, where residues at both terminals contributed equally, *i.e.,* residues 897 to 917 at N terminal and residues 962 to 984 at C terminal. However, predictor of natural disordered regions pool predictors have predicted high propensity while other predictors have shown moderate disorder propensity (Fig. S1). Further, the all-atom MD simulation was carried out to gain further insight into the structural dynamics of a c-Myc peptide isolated from the MAX

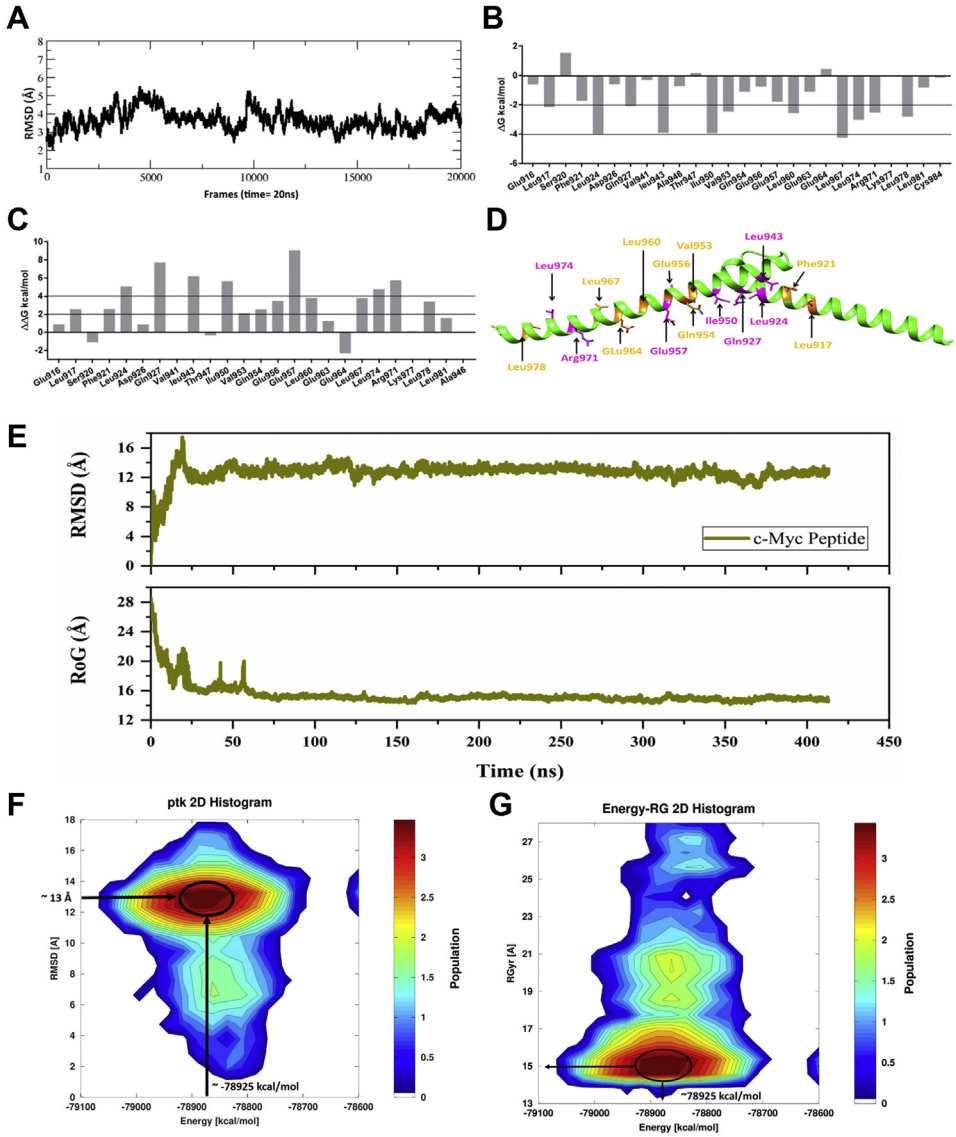

Figure 1. Identification of hot spot residues present on the c-Myc/MAX interface and generation of different c-Myc ensembles. *A*, schematic representation of c-Myc/MAX complex root mean square deviation (RMSD) during 20 ns of molecular dynamics simulation. *B*, free energy contribution of interface residues in c-Myc/MAX dimer. *C*, c-Myc/MAX dimer hot spot binding free energy decomposition using MM-PBSA *in silico* alanine scanning mutagenesis. *D*, map of the energetically important hot spots and warm spots residues in c-Myc/MAX interface region. For clarity purpose only c-Myc structure is shown. *E*, 412 ns extensive MD simulation showed a stable RMSD and RoG values for Cα backbone of c-Myc. *F* and *G*, 2D histogram plots of simulation trajectories with variable RMSD *versus* energy (*F*) and RoG *versus* energy (*G*). MAX, MAX, Myc-associated factor X; MM-PBSA, molecular mechanics Poisson–Boltzmann surface area; RoG, radius of gyration.

bound structure (PDB ID—1NKP). As observed in extensive simulations of ∼410 ns, the c-Myc structure loses helical composition and gains random coil conformation, primarily in its leucine-zipper motif region. Based on RMSD calculation, the structure showed higher deviations in the initial 25 ns and gained deviations up to 16 Å from 4 Å and then dropped minimally at 12 Å for the rest of the simulation period with minor variations (Fig. 1*E*). Similar trends were seen in the radius of gyration (RoG) analysis. Overall, this shows that the structure gains a stable conformation (Fig. 1*E*).

Conformation ensemble of c-Myc for docking

Here, the rigorous MD simulation up to ∼410 ns of c-Myc structure yielded over 400 thousand conformations, sufficient to identify stable conformations. The RMSD and RoG plots were stable after 50 ns of simulation. These conformations were then mapped on two 2D histogram plots by considering RMSD and RoG concerning energy values from the simulations. As depicted in Figure 1*F*, the simulation frames are charted as RMSD *versus* energy, where the densest areas show the high population of frames on a scale of 0 to 3.5 with distinguished colors. All frames were found to have lied within a range of energy −79,100 to −78,600 kcal/mol and RMSD 1 to 18 Å. The higher number of frames with nearly identical parameters (encircled and arrowed at x- and y-axes in Fig. 1*F*) were found with RMSD 13 Å and energy approximately −78,925 kcal/mol. A similar analysis was performed with RoG and energy parameters, where the high population of frames was found with RoG 15 Å and energy

approximately −78,925 kcal/mol (Fig. 1*G*). Then, based on these two sets of values, nearly 380 frames were identified, falling in the calculated ranges. Two frames at 170.23 ns (F1; obtained from RoG *versus* energy) and 326.37 ns (F2; obtained from RMSD *versus* energy) were finally chosen through manual inspection and were used for ensemble docking.

Molecular docking led to the identification of hit candidate molecules

High-throughput virtual screening (HTVS) has proven to be a distinctive approach in drug discovery because of certain benefits like time saving and cost-effectiveness. Hence, here we have screened nearly 30,000 compounds from the protein–protein interaction-focused library from Life Chemicals Inc against the two conformations (F1 and F2) of c-Myc. The *LigPrep* module generated 54,413 structures, which were screened through HTVS, standard precision (SP), and extra precision (XP) mode of docking. First, 30% of best scoring compounds were passed from HTVS to SP and SP to XP mode, and then 50% of compounds were passed for molecular mechanics generalized Born surface area (MM-GBSA) calculation. With this, nearly 12,000 binding poses of all compounds were produced for both frames. Next, all the compounds were visually inspected for their molecular interaction with the identified hot spot and warm spot, all together with docking score and binding energy. Finally, seven compounds were purchased that showed appreciable binding and interaction with the hot spot residues against both the frames (F1 and F2) (Table S5). The ligand interaction analysis showed that among the identified hot spot and warm spot, the seven compounds commonly interacted with the Gln954, Glu956, and Glu957 residues of Frame-F1 (Fig. S2) and with residues Val953, Gln954, Glu956, and Glu957 of Frame-F2 (Fig. S3). Moreover, in both the frames, the compounds also interacted with residues Arg970 and His976, shaping the neighborhood of the hot spot and warm spot residues. The MM-GBSA scores (binding energy) of all complexes fall within a range of −20 to −50 kcal/mol. Collectively, the selected seven compounds showed substantial binding affinity against both the frames, which was plausible due to their interactions with the defined hot spot and warm spot residues.

The compounds showed noteworthy in vitro potency and induced apoptosis in cell lines showing endogenous c-Myc expression

Based on the docking score and binding energy, we purchased seven compounds from Life Chemicals and studied their *in vitro* anticancer potential. Three c-Myc expressing cells were incubated with different concentrations of the purchased compounds and incubated for 48 h. Among the seven studied compounds, three compounds, *i.e.,* F1288-0026, F2018-1398, and F2504-0393, did not show appreciating anticancer property, with an IC_{50} value of more than 15 μM (Fig. 2). One of the compounds, *i.e.,* F1132-0721, showed a higher IC_{50} value against the two-cell line, while showed a relatively low IC_{50} value against HT-29, *i.e.,* 2.48 ± 0.41 μM (Fig. 2). The rest of the three compounds, *i.e.,* F0909-0073, F0909-0360, and F1021-0686, displayed significant anticancer potential in a dose-dependent manner against the three c-Myc-expressing cell lines (Fig. 2). The IC_{50} value for these three compounds was in the range of 0.209 ± 0.094 to 3.21 ± 0.75 μM, which was comparatively lesser than the reported c-Myc inhibitor, 10074-G5 (from our previous work, (34)). These three compounds were further studied on low-Myc expressing and noncancerous transformed cell lines, *i.e.,* U-87 MG and HEK-293T, respectively. From Figure 3*A*, it can be inferred that these three compounds showed less cell-killing potential toward the U-87 MG and HEK-293T, which is evident from its high IC_{50} value (Fig. 3*A*). Based on appreciable cell-killing potential, these three compounds, *i.e.,* F0909-0073, F0909-0360, and F1021-0686, were further studied to gain more insight into their antioncogenic potential. Further, the Annexin V/PI apoptosis assay showed that the three compounds induce apoptosis in the c-Myc expressing cell, HT-29. As depicted from Figure 3*B*, nearly 36%, 39%, and 43% of the cell population was in apoptotic quadrants when treated with 10 μM of F0909-0073, F0909-0360, and F1021-0686, respectively, for 24 h.

The compounds efficiently inhibit the functionality of c-Myc

To understand whether the cell death induced by the three molecules involves the inhibition of c-Myc functionality, we studied the change in expression of c-Myc target genes (CAD, ODC1, NOP58, and NOP56 (35, 36)) both at the transcriptional and translational levels. After treating the D341 and HL-60 cell lines with different concentrations of the three-hit compounds, 1 μg of RNA was used for cDNA synthesis, which was later used for qPCR. For both cell lines, the qPCR data showed a significant decrease in the mRNA expression level of all the c-Myc target genes with increasing concentrations of all the compounds compared to untreated cells (Fig. 4*A*). Further, the protein level of c-Myc target genes (CAD, NOP58, and ODC1) was also analyzed after treating the D341 cell with increasing concentrations of the three-hit compounds for 36 h. Similar to the qPCR data, the Western blot analysis showed that the treatment of these three compounds leads to the translational repression of all the target genes (Fig. 4*B*). After the treatment with the compounds, a dose-dependent significant decrease in protein band intensity was observed for all the three c-Myc target genes. Thus, the qPCR and Western blot analysis indicated that the three compounds could inhibit Myc's function and therefore repression in Myc target genes was observed both at mRNA and protein level. Further, an array of c-Myc target genes were studied for the change in mRNA expression after the treatment with the compounds. The gene array analysis after the treatment of the compound is summarized in Figures 5 and S4. As seen from Fig. S4, the treatment with the compounds led to the change in mRNA expression of c-Myc target genes. The treatment of all three compounds showed a similar trend in the mRNA expression of the majority of the target genes. The heatmap shown in Figure 5*A* shows the expression fold change of the target gene mRNA compared to the untreated cells. Further, the scattered plot (Fig. 5, *B–D*) and the volcano plot

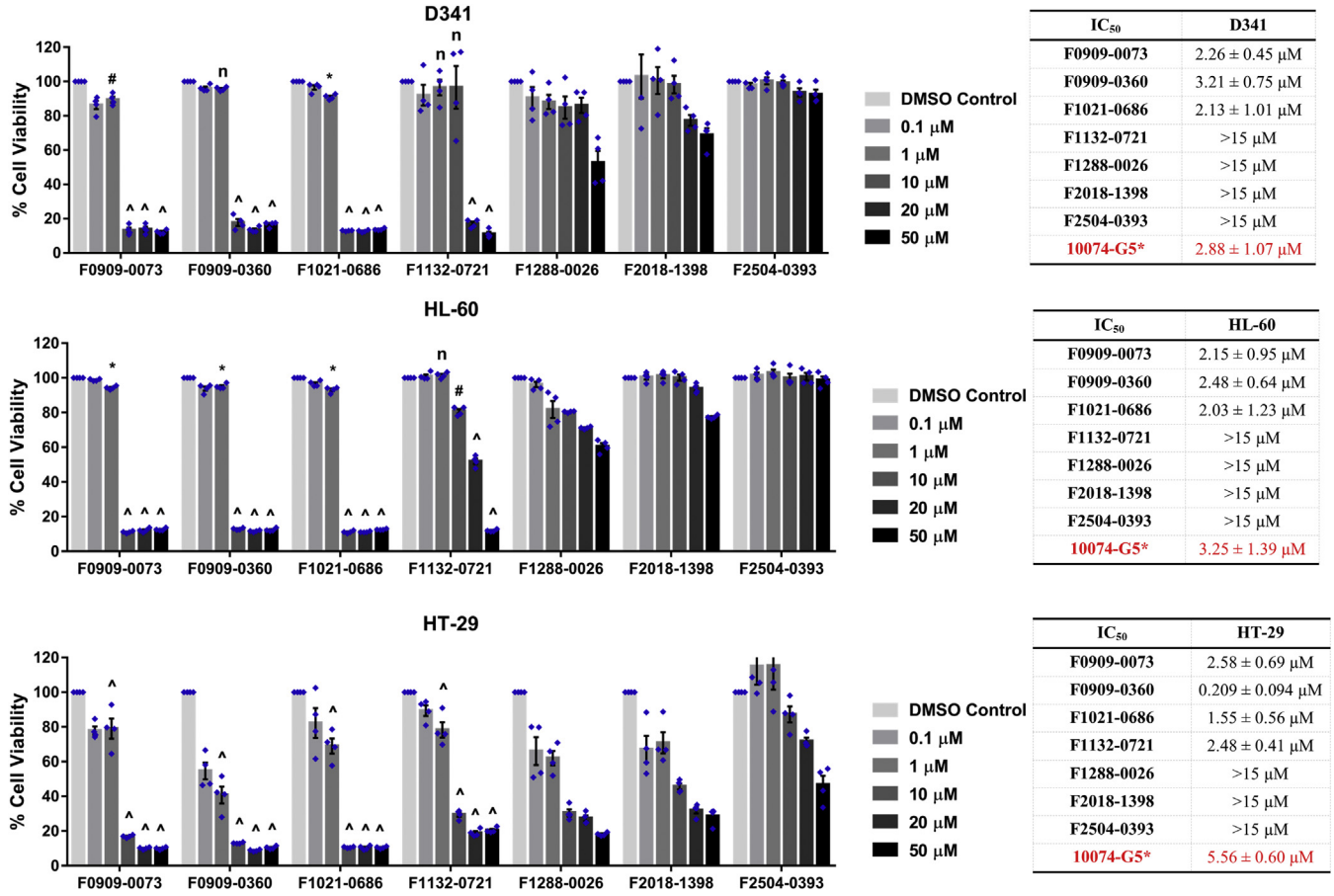

IC_{50}	D341
F0909-0073	2.26 ± 0.45 μM
F0909-0360	3.21 ± 0.75 μM
F1021-0686	2.13 ± 1.01 μM
F1132-0721	>15 μM
F1288-0026	>15 μM
F2018-1398	>15 μM
F2504-0393	>15 μM
10074-G5*	2.88 ± 1.07 μM

IC_{50}	HL-60
F0909-0073	2.15 ± 0.95 μM
F0909-0360	2.48 ± 0.64 μM
F1021-0686	2.03 ± 1.23 μM
F1132-0721	>15 μM
F1288-0026	>15 μM
F2018-1398	>15 μM
F2504-0393	>15 μM
10074-G5*	3.25 ± 1.39 μM

IC_{50}	HT-29
F0909-0073	2.58 ± 0.69 μM
F0909-0360	0.209 ± 0.094 μM
F1021-0686	1.55 ± 0.56 μM
F1132-0721	2.48 ± 0.41 μM
F1288-0026	>15 μM
F2018-1398	>15 μM
F2504-0393	>15 μM
10074-G5*	5.56 ± 0.60 μM

Figure 2. The compounds showed appreciable anticancer activity against the three c-Myc expressing cell lines. Cytotoxicity profile of top selected compounds against c-Myc expressing cell lines. Bars represent mean ± SEM of four independent experiments (*p*-value *versus* DMSO control. $^{*}p < 0.05$, $^{\#}p < 0.001$, $^{\wedge}p < 0.0001$, n=nonsignificant). The IC_{50} value of all the compounds along with 10074-G5 is given adjacent to the respective cell lines. Values represent mean ± SEM of four independent experiments.

(Fig. 5, *E–G*) for normalized gene expression were shown individually for the three compounds.

The compounds showed considerable in vitro *efficacy against cancer stem cells*

The CSC, *i.e.,* CD133+ cell population, was isolated from the D341 cell lines using the magnetic-activated cell sorting (MACS) methods. The isolated CD133+ (D341-CSCs) cells were further maintained by culturing in low-attachment plates with a serum-free medium. To characterize CD133+ cells, we studied the expression of CSC markers (CD133, SOX2, Oct4, Nanog, and c-Myc) using qPCR and Western blot. The transcriptional and translational studies showed a significant increase in the CSC markers compared to the D341 cells (Fig. 6, *A–C*). The single-cell suspension isolated from the D341-CSC tumorsphere was treated with various concentrations of the three-hit compounds along with the reported c-Myc inhibitor, 10074-G5. Figure 6*D* shows that after 48 h of treatment, all three compounds showed appreciable cell-killing potential against the D341-CSCs. These three compounds showed dose-dependent response with noticeable IC_{50} values in lower micromolar range *viz.* 6.32 ± 2.82, 4.06 ± 0.65, and 5.27 ± 4.26 μM for F0909-0073, F0909-0360, and F1021-0686, respectively. On the other hand, the reported c-Myc inhibitor, *i.e.,* 10074-G5, did not display cytotoxicity toward the D341-CSCs. Similarly, the three-hit compounds, along with 10074-G5, were studied for their potential to restrict the sphere-forming potential of the D341-CSCs. The single-cell suspension of D341-CSCs was incubated with 10 μM concentration of compounds and was incubated for 7 days. From Figure 6*E*, it can be seen that all the compounds showed excellent potential in restricting the sphere formation in D341-CSCs. The three hit compounds, *i.e.,* F0909-0073, F0909-0360, and F1021-0686, showed a reduction of 73.5%, 98.5%, and 97%, respectively, in the tumorsphere formed from the D341-CSCs. On the contrary, the reported c-Myc inhibitor, 10074-G5, did not display the potential to restrict the sphere-forming capacity of the D341-CSCs.

The binding of compounds resulted in the quenching of intrinsic tryptophan fluorescence

Taking advantage of the incorporated tryptophan (Trp) residue in place of tyrosine in the synthesized c-$Myc_{910-960}$ peptide, we employed fluorescence spectroscopy to investigate any change in Trp fluorescence intensity or stokes shift in the presence of the compounds, which will substantiate the formation of Myc-compound complex. The black dotted line in Figure 7*A* represents the steady-state intrinsic fluorescence of

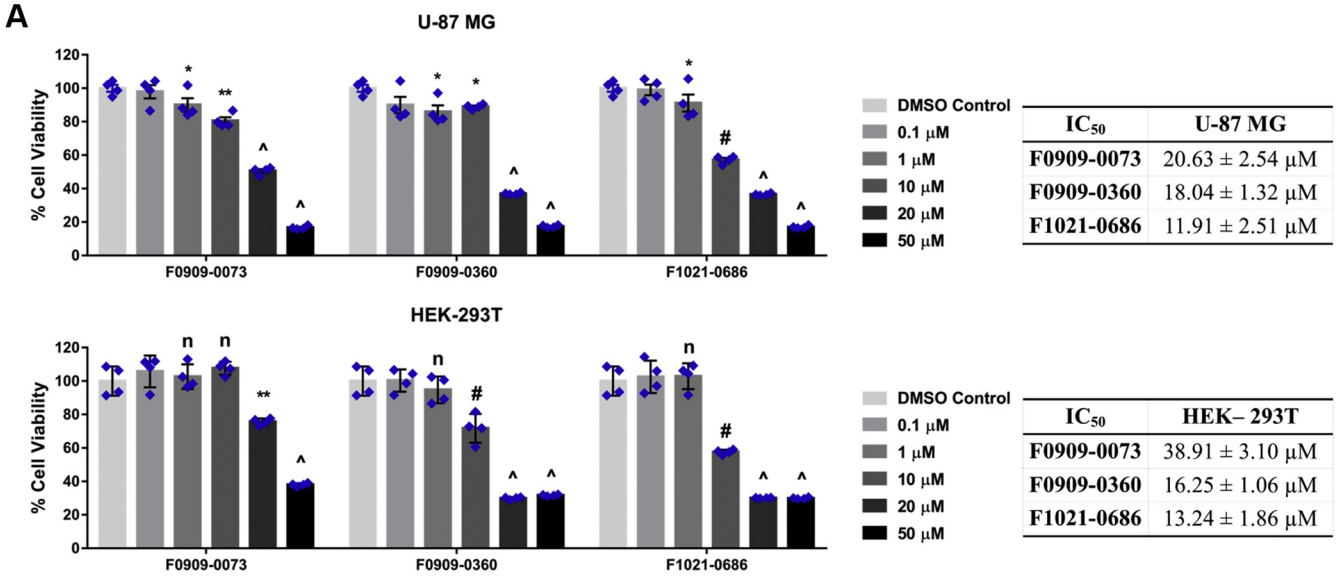

IC_{50}	U-87 MG
F0909-0073	20.63 ± 2.54 μM
F0909-0360	18.04 ± 1.32 μM
F1021-0686	11.91 ± 2.51 μM

IC_{50}	HEK– 293T
F0909-0073	38.91 ± 3.10 μM
F0909-0360	16.25 ± 1.06 μM
F1021-0686	13.24 ± 1.86 μM

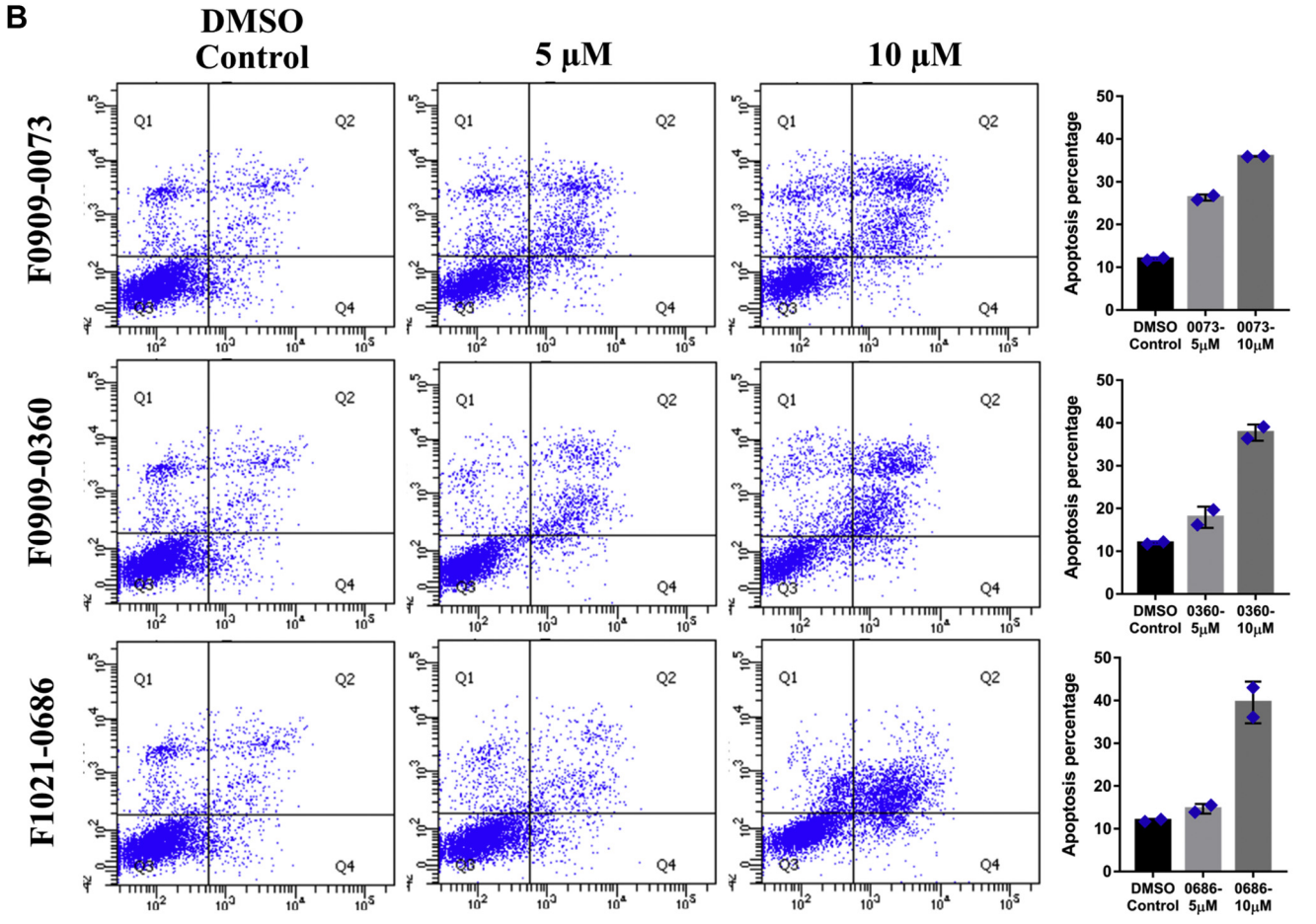

Figure 3. The top three compounds showed c-Myc-dependent apoptotic cell death. *A*, anticancer profile of the top three compounds against the non-c-Myc expressing (U-87 MG) and noncancerous (HEK-293T) cells. Bars represent mean ± SEM of four independent experiments (*p*-value *versus* DMSO control. $^{*}p < 0.05$, $^{**}p < 0.01$, $^{\#}p < 0.001$, $^{\wedge}p < 0.0001$, n=nonsignificant). The IC50 value of all the three compounds is given adjacent to the respective cell lines. Values represent mean ± SEM of four independent experiments. *B*, the three compounds induce apoptosis in c-Myc expressing cell line, HT-29. The cells were treated with different concentrations of the compounds for 24 h and then probed with Annexin V and propidium iodide. The percentage of cells after compound treatment is depicted as bar graph. The shown data are part of a single experiment, so the same DMSO control data are presented and compared with all the compounds.

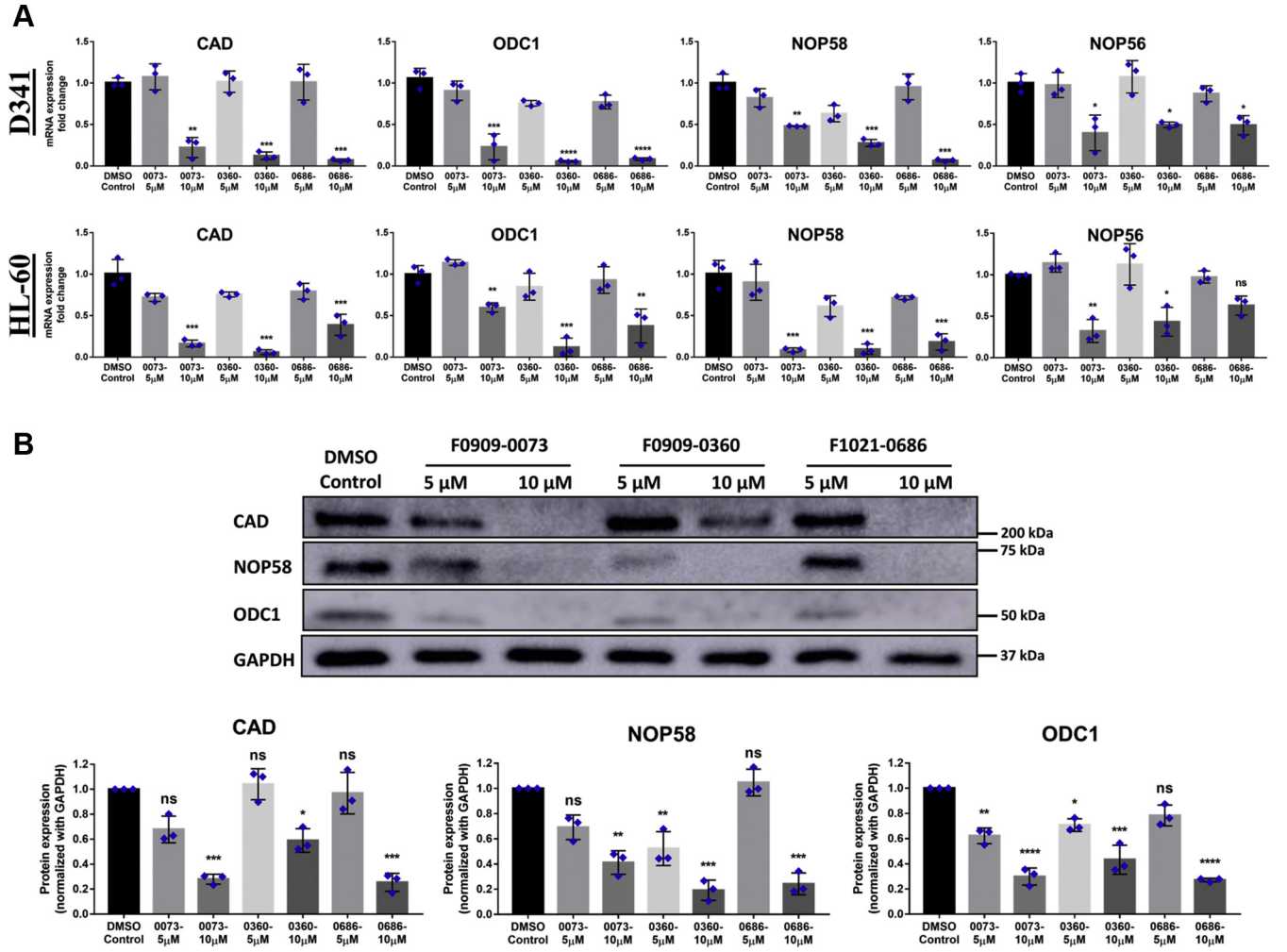

Figure 4. Treatment of the three compounds led to the functional repression of c-Myc target gene. *A*, the mRNA expression level of c-Myc target genes (CAD, ODC1, NOP58, and NOP86) after treatment with different concentrations of the compounds on 2 cell lines. Bars represent mean ± SD of three experimental replicates (*p*-value *versus* DMSO control. *$p < 0.05$, **$p < 0.01$, ***$p < 0.001$). *B*, decrease in protein level of c-Myc target genes were observed after treating with different concentrations of the compounds. Quantified change in protein level of c-Myc target genes after treatment is shown below the blot. Bars represent mean ± SD of three experimental replicates (*p*-value *versus* DMSO control. *$p < 0.05$, **$p < 0.01$, ***$p < 0.001$, ****$p < 0.0001$, ns = nonsignificant).

Trp residue of c-Myc on excitation at 295 nm wavelength (λ_{max} at 350 nm). As inferred from Figure 7*A*, the intrinsic fluorescence emission of c-Myc Trp decreases with increasing concentrations of compound F0909-0360 from 0.01 μM to 1 μM. A similar trend is observed on fluorescence intensity of c-Myc with other compounds F0909-0073 and F1021-0686. This suggests the alterations occurring in the spatial arrangement of the aromatic amino acid in the c-Myc peptide due to the interaction with compounds. Additionally, to draw a comparison, the effect of a well-known inhibitor compound 10074-G5 (control) on intrinsic tryptophan fluorescence intensity of c-Myc is also studied alongside. Figure 7*A* depicts a similar decrease in fluorescence intensity of c-Myc by the reported inhibitor 10074-G5. The decreasing transitions in fluorescence intensities of c-Myc are analogous to as produced by the known inhibitor are indicative of the quenching of Trp fluorescence by compounds, and consequently, the interaction of all three compounds with c-Myc peptide. The fluorescence emission of c-Myc Trp residue in presence of the compounds was studied by Stern–Volmer plot (Fig. 7*A*). As seen from the figure, a linear pattern was observed at lower concentrations, which bends downwards reflecting the plateau phase in quenching process.

The binding of the compounds resulted in a time-resolved decrease in Trp fluorescence lifetime

Further, we have measured the changes occurring in the fluorescence lifetime of Trp residue in the c-Myc$_{910\text{-}960}$ peptide on interaction with the studied compounds. The average fluorescence lifetime of c-Myc Trp residue in the presence of 20 mM sodium phosphate buffer (pH 7.4) is documented to be 2.5 ns. The average lifetime plotted against the compound concentrations in Figure 7*B* illustrates their effect on fluorescence decay of Trp residue. As the concentration of compounds is increased, a substantial dip in fluorescence lifetime is detected. This noticeable downward trend in fluorescence lifetime is observed for all the studied compounds, including control (10074-G5). In the presence of the lowest

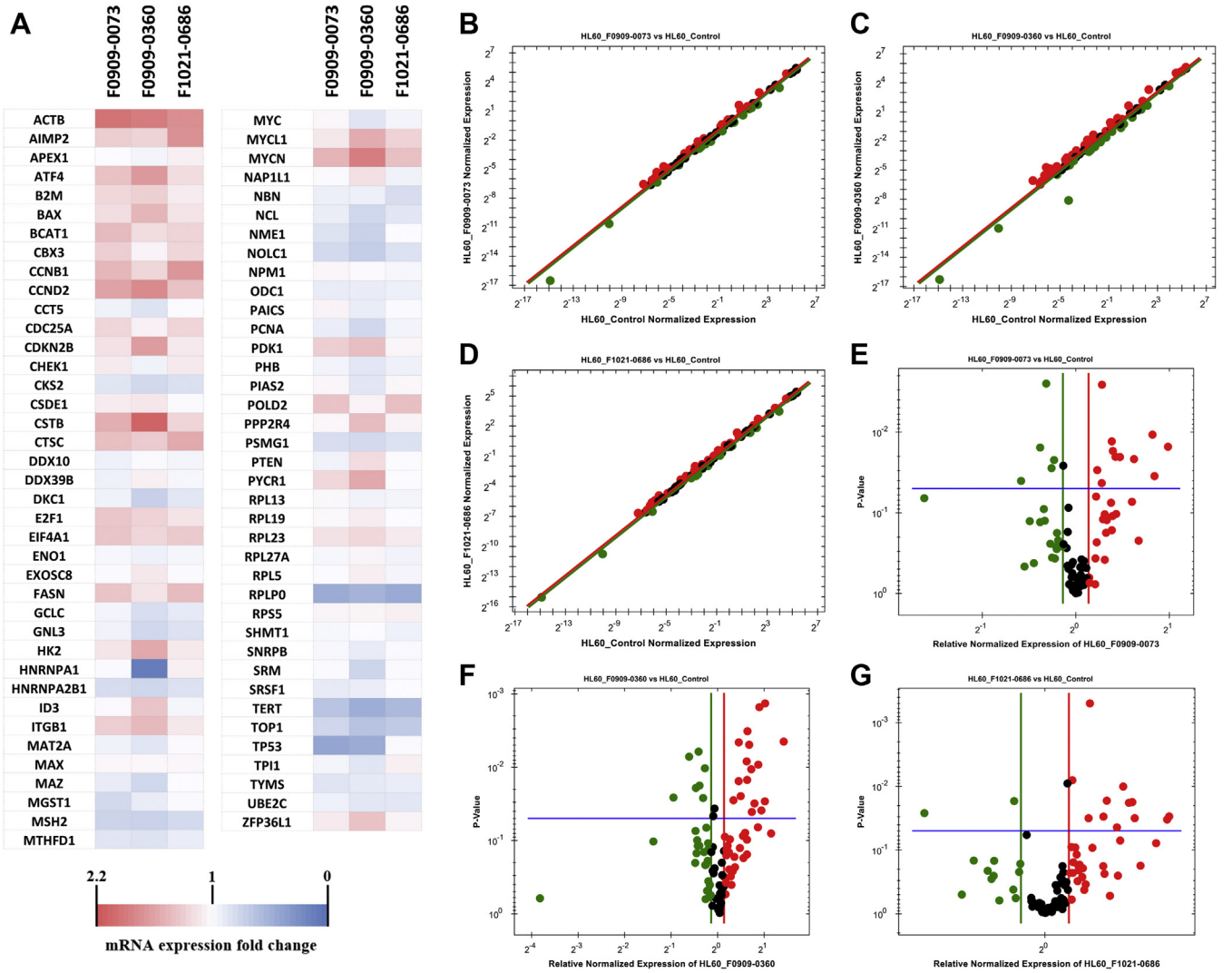

Figure 5. Gene array analysis of c-Myc target genes after the compound's treatment. *A*, heatmap diagram showing the change in c-Myc target gene mRNA after the treatment with the compounds (n = 2) relative to the untreated HL-60 cells. *B–D*, scatter plot analysis of the gene array results of the three compounds *versus* untreated cells. Each dots represent a single gene, and upregulation is represented with *red dots* and the downregulation is represented with *green dots*. The regulation threshold was assigned as 1.10-fold to create the boundary. *E–G*, volcano plot analysis represent the relative normalized expression of the gene array data of the three compounds *versus* untreated cells. The color code is same as in scatter plot. The boundary value was assigned as 1.10-fold regulation threshold, and the *p*-value of 0.05 was considered and represented in each plot.

concentration of compounds (5 μM), the average lifetime is decreased from 2.5 ns to 2.01 ns, 2.02 ns, and 2.35 ns, whereas on the addition of 25 μM of compounds, it diminishes to 1.59 ns, 1.74 ns, and 1.77 ns for F0909-0360, F1021-0686, and F0909-0073 compounds, respectively. Likewise, for 25 μM of the control compound, 10074-G5, the average lifetime of Trp declines to 1.72 ns. The time-resolved fluorescence decay of Trp residue in the presence of different concentrations of compounds is shown in Figure 7*B*. Further, the change in the average lifetime of Trp because of the binding of ligands is also reflected in the τ_1, τ_2, and τ_3 components, which are tabulated in Table S6. These outcomes validate the interaction of the studied compound with the c-Myc peptide.

Compound binding led to a decrease in c-Myc disorderness

The conformational dynamics of c-Myc on binding with the studied compounds are analyzed using circular dichroism (CD) spectroscopy. As reported earlier, c-Myc exhibits a prominent negative peak at ∼200 nm in far-UV CD spectra; it is intrinsically disordered and forms ensembles of structures. Further, Figure 7*C* represents the CD spectra of c-Myc in the presence of compounds F0909-0360, F0909-0073, and F1021-0686, respectively. The results in Figure 7*C* indicate that c-Myc remains unstructured on interaction with all three investigated compounds. The reduction in negative ellipticity from -8 mean residue ellipticity to -4 mean residue ellipticity at 200 nm of c-Myc on the addition of the 5 μM compounds signifies the binding of the compounds with the disordered c-Myc. However, the binding of the compounds with the c-Myc does not lead to the transition to α-helix or β-sheets, which is evident from the absence of the negative peak at 208 nm and 222 nm (α-helix) and 218 nm (β-sheets) after incubation with the compounds.

MD simulation showed a stable protein–ligand complex

MD simulations were performed up to 200 ns for each complex to confirm the binding stability of protein–ligand

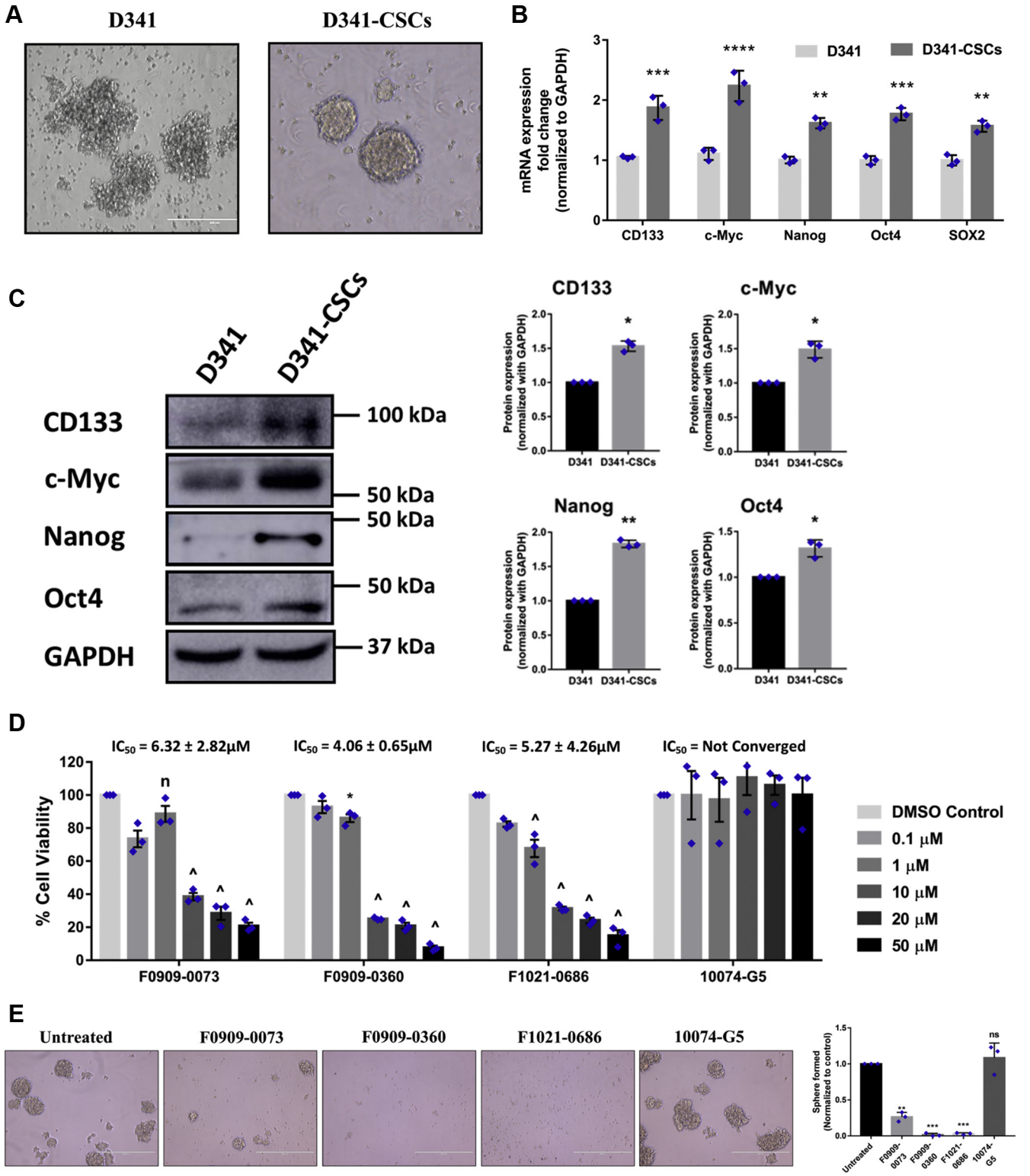

Figure 6. The three compounds efficiently restrict of growth and sphere forming capacity of D341-CSCs. characterization of cancer stem cells isolated from D341 cell lines. *A*, microscopic images of D341 cancer and D341 cancer stem cells (scale bar = 400 μm). *B*, the change in mRNA level of CSC markers were quantified using quantitative PCR. Bars represent mean ± SD of three experimental replicates (*p*-value *versus* D341 cells. $^{**}p < 0.01$, $^{***}p < 0.001$, $^{****}p < 0.0001$). *C*, the protein level of CSC markers was probed using Western blot. Bars represent mean ± SD of three experimental replicates (*p*-value *versus* D341 cells. $^{*}p < 0.05$, $^{**}p < 0.01$). *D*, cytotoxicity profile of the three compounds on D341-CSCs showed a dose-dependent response. While the known c-Myc inhibitor, 10074-G5 showed not cytotoxicity at all. Bars represent mean ± SEM of three independent experiments (*p*-value *versus* DMSO control. $^{*}p < 0.05$, $^{\wedge}p < 0.0001$, n=nonsignificant). *E*, the compounds substantially restrict the sphere-forming property of D341-CSCs as contrary to the 10074-G5 inhibitor (scale bar = 400 μm). Bars represent mean ± SD of three experimental replicates (*p*-value *versus* D341 cells. $^{**}p < 0.01$, $^{***}p < 0.001$, ns=non-significant). CSC, cancer stem cell.

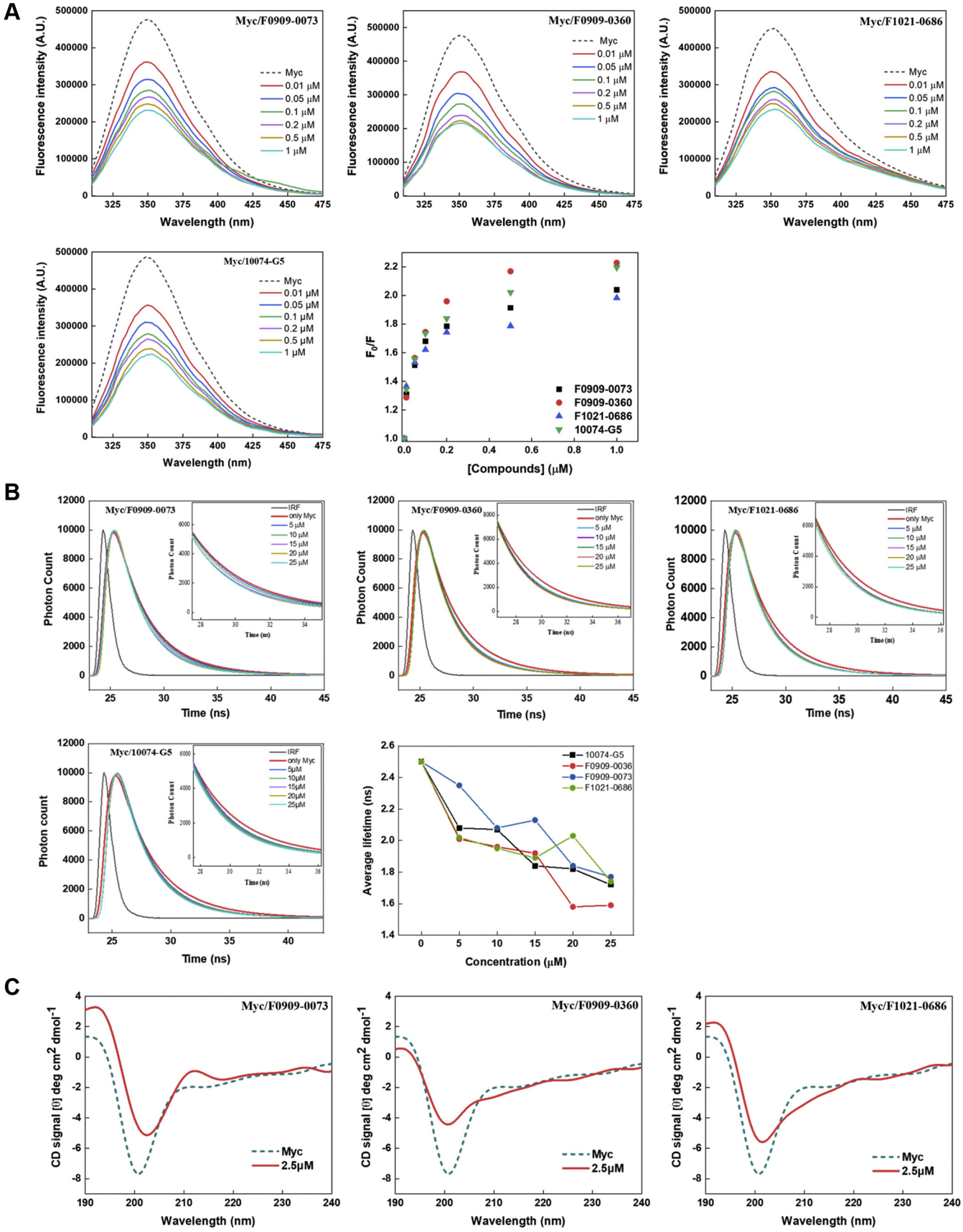

Figure 7. The three compounds showed efficient binding with the disordered c-Myc$_{910-960}$ peptide and resulted in overall conformational change. *A*, fluorescence spectroscopy data showed a decrease in intrinsic Trp fluorescence of the c-Myc$_{910-960}$ peptide with increasing concentration of the three compounds and the known c-Myc inhibitor, 10074-G5. Stern–Volmer plot of the fluorescence response of c-Myc to the compounds. *B*, the graphs represent

complexes. We identified three compounds (F0909-0073, F0909-0360, and F1021-0686) from experimental validations against c-Myc protein where these compounds have shown remarkable inhibition efficiency with up to nanomolar IC_{50} values. All these compounds were tested for binding stability with both frames of c-Myc (F1 and F2). Based on RMSD values of c-α atoms of c-Myc-F1 upon binding with compounds, the variation in mean atomic distances was 16.6 Å, 12.5 Å, 11.5 Å for F0909-0073, F0909-0360, and F1021-0686, respectively (Fig. S5*A*). The RMSD plots are observed to be stabilized after 50 ns, and initial fluctuations may be due to structural changes of c-Myc being an IDP. However, the heavy fluxes in RMSD up to ∼14 Å can be observed in the unbound conformation of protein till half of the simulation period. The mean root mean square fluctuation (RMSF) plots show structural changes in the simulation of unbound and compound-bound c-Myc conformations (Fig. S5*B*). According to trajectory analysis, the compounds F0909-0073 and F1021-0686 show a slight fluctuation in a few frames during the simulation period, which stabilized later. At the same time, F0909-0360 is tightly bound to the c-Myc-F1 throughout the simulations. As given in Fig. S7, the hydrophobic interactions *via* water and ionic bridges are seen for a major fraction of simulation time. The simulation interaction timelines also represent the same concerning the time where the interaction with Glu957 is intact during the entire simulation period except for a few fluctuating frames (Fig. S6).

According to the simulations of c-Myc-F2 in complex with experimentally validated compounds, F0909-0073 and F0909-0360 have shown strong binding throughout the simulations, but F1021-0686 has experienced some fluctuations. No such noticeable changes were observed in the simulation of unbound and compound bound conformations of c-Myc-F2. The average RMSD of C-α atoms of c-Myc-F2 are 16.8 Å, 15.8 Å, and 13.5 Å in complex with F0909-0073, F0909-0360, and F1021-0686, respectively (Fig. S5*C*). Similarly, RMSF values were also high of C-α atoms of c-Myc-F2 in complex with F1021-0686 compared to F0909-0073, F0909-0360 bound c-Myc-F2 (Fig. S5*D*). As per Fig. S6, multiple new interactions in addition to existing ones were formed during simulations, but the interaction of F1021-0686 with Glu957 remained intact for most of the simulation time.

Discussion

PPI plays a crucial role in various biological processes, and its perturbation is related to various disease conditions, including cancer (4, 5, 7). The involvement of PPIs in various diseases provides an open scope for developing new clinical therapeutics targeting perturbated PPIs. Despite its role in various disease states, screening a small-molecule inhibitor is quite challenging because of the PPI interface's large, pocketless, and hydrophobic features (1, 37, 38). However, the structural insight in the PPIs has been proven considerably in the clinical development of novel PPI inhibitors. In particular, identifying hot spots has revolutionized the discovery of small-molecule inhibitors against perturbated PPIs. The c-Myc/MAX heterodimer is considered a hot target for cancer therapeutics as it is linked to nearly 75% of human cancer showing aggressive nature and resistance toward available chemotherapy (17, 18). The PPI interface of c-Myc is not well characterized, and therefore, we first identified the hot spot residues, which have a substantial contribution in c-Myc and MAX dimerization. The hot spots of PPIs could be identified using different computational approaches such as a simple free energy-based method (*e.g.,* Robetta server (39)), machine learning-based methods (*e.g.,* KFC server (40)), and MD simulation-based methods (*e.g.,* MM-PBSA alanine scanning mutagenesis (41)). However, MD simulation–based MM-PBSA methods are commonly used to identify hot spot residues in the PPI interface region as these methods are more reliable and correlate well with the experimental results.

The scientific community acknowledges the per-residue energy decomposition and ASM methods to detect hot spots in a target PPI (42–44). Combining these two techniques has accurately identified the free energy contributing residues by simultaneously mutating the residues to alanine and calculating the decrease in free energy of binding (ΔΔG) after mutation. After simulating the c-Myc/MAX complex for 20 ns, the last 4000 frames were used to calculate binding free energy decomposition using the MM-PBSA method. The high binding free energy value (−115.85 kcal/mol) for the c-Myc/MAX dimer indicates the stability of the complex, which is possible due to the large interface region. Further, the per-residue energy decomposition was estimated using the MM-PBSA method, which implies the individual contribution of the interface residues to the total binding free energy of the complex. Eleven interface residues showed more than −2.0 kcal/mol contribution to the c-Myc/MAX heterodimer (Fig. 1*B*). After the total binding free energy and per-residue energy decomposition analysis, the *in silico* ASM was employed on the same 4000 frames previously used to estimate free energy decomposition. After mutating the individual interface residue with alanine, the change in free energy of binding (ΔΔG) was calculated, and the residues were categorized into hot, warm, and null spots (Fig. 1*C* and Table S4). The characterization was based on three criteria: (a) those residues whose mutation resulted in more than 4 kcal/mol of ΔΔG were classified as "hot spots." These residues are deeply embedded and protected from the solvent exposure at the interface and play a crucial role in the structural stability of the protein-protein complex; (b) those residues whose mutation resulted in more than 2 to 4 kcal/mol of ΔΔG were classified as "warm spots" which plays a modest role in the structural stability of the protein-protein complex, and (c) those residues

the fluorescence lifetime decay measurement of c-$Myc_{910-960}$ peptide with different concentrations of the three compounds, and the known c-Myc inhibitor, 10074-G5. Decrease in average fluorescence lifetime decay of Trp residue in the presence of three compounds and 10074-G5 was shown in last. *C*, binding of the compounds with the c-$Myc_{910-960}$ peptide resulted in decreased of disorderness. The CD spectra of $Myc_{910-960}$ peptide showed a decrease in negative ellipticity when incubated with 5 μM each three compounds. CD, circular dichroism; Trp, tryptophan.

whose mutation resulted in less than 2 kcal/mol of ΔΔG were classified as "null spots" having most minor contribution in the structural stability of PPIs. Based on these criteria, seven and nine residues on the surface of c-Myc are classified as hot spots and warm spots, respectively (Fig. 1*D* and Table S4).

The dynamic nature of the IDPs provides structural flexibility to interact with various partners, thereby expanding the functional paradigm (26, 45). Its abundance in the eukaryotes and structural flexibility is directly linked to its involvement in the disease phenotype. Targeting IDPs with small-molecule inhibitors provides a profound strategy for clinical therapeutics; however, the structural heterogeneity of the IDPs is an inherent challenge of using them as a druggable target. In PPI, the disordered protein regions usually display ordered transition and perform diverse functions. Therefore, it was of utmost importance to understand the dynamic nature of the target protein, c-Myc. The mean of the result obtained from various online disorder tools predicted 50% disorder propensity in the bHLH-LZ domain of c-Myc, which was equally contributed by the N- and C-terminal residues (Fig. S1). Furthermore, the extensive all-atom MD simulation (∼410 ns) of the c-Myc isolated from the crystal structure revealed the loss of helical conformation to the random coil structure (Fig. 1*E*).

Ensemble docking is a valuable and helpful asset for drug discovery against IDPs, and particularly in the case of PPI, its applications are widespread (46, 47). Generally, MD simulations are performed to capture conformations of a target protein at different time frames to identify potential hits through docking (46). Over 4 lakhs of the generated conformers obtained from the ∼410 ns MD simulation were used to identify structure ensembles by mapping them on two 2D histogram plots by considering RMSD and RoG with respect to energy values from the simulation conformations (Fig. 1, *F* and *G*). Finally, approximately 380 frames were identified, falling in the calculated ranges, and two frames, *i.e.,* at 170.23 ns (F1) and 326.37 ns (F2), were finally chosen for ensemble docking. The structure-based virtual screening was employed against the identified hot spot and warm spot residues to screen the PPI-focused library with approximately 30,000 compounds for both the chosen c-Myc frames. We visually inspected the binding poses following molecular docking and ligand–protein binding energy to identify the top hit molecules based on the individual interactions with the hot spot and warm spot residues. Seven compounds that showed noteworthy docking score, binding energy, and interaction with the target residues on the F1 and F2 frames were finally chosen for further experimental validation (Table S5). Among the identified hot spot and warm spot residues, Val953, Gln954, Glu956, and Glu957 of both the frames were found to noncovalently interact with the finalized seven compounds (Figs. S2 and S3).

c-Myc aberrant expression is associated with various human cancers showing aggressive nature. In our previous study, we reported the same and found that the expression of c-Myc mRNA was significantly high in various cancer, and its expression is inversely linked with overall patient survival thus, suggesting its prognostic and therapeutic role in human cancers (34). The *in vitro* anticancer potential of the purchased compounds was studied *via* 3-(4,5-dimethylthiazol-2-yl)-2,5-diphenyltetrazolium bromide (MTT)-based cell-cytotoxicity experiments against three cell lines characterized for endogenous expression of c-Myc in our previous study. Among the seven purchased compounds, three compounds, *i.e.*, F0909-0073, F0909-0360, and F1021-0686, showed substantial cytotoxicity potential against the three studies cell lines with significant IC_{50} values ranging from 0.209 ± 0.094 to 3.21 ± 0.75 μM (Fig. 2). The three compounds were more effective than the known c-Myc inhibitor as the IC_{50} values of the compounds were found to be comparatively lesser than 10074-G5 (Fig. 2). Additionally, the specificity of these top potent compounds toward c-Myc can be realized by their less cell killing and high IC_{50} values against the non-c-Myc expressing cells (U-87 MG) and noncancerous cells (HEK-293T) (Fig. 3*A*). The anticancer data suggests that three out of the seven identified compounds showed appreciable *in vitro* potency and were able to induce apoptotic cell death in cells showing endogenous expression of c-Myc (Fig. 3*B*).

The vast functional landscape of c-Myc encompasses the regulation of several genes, which contribute to the oncogenic phenotype. To confirm that the apoptotic cell death mediated by the three compounds involves the regulatory inhibition of c-Myc, we studied the change in expression of c-Myc target genes (CAD, ODC1, NOP56, and NOP58 (35, 36)) at the transcription and translation level. The qPCR and Western blot data suggested a dose-dependent decrease in the expression level of the target genes when treated with varying concentrations of the three compounds (Fig. 4). Comparing the change in the target gene expression level after treatment with the compounds and 10074-G5 from our previous study (34), it was worth noticing that the decrease in expression after the compound's treatment was far much more than after treatment with 10074-G5 even when used at higher concentrations. Further, we performed the PrimePCR array on c-Myc target genes to analyze the change in mRNA expression after treating the compounds. A total of 67 c-Myc target genes were studied, and the data showed that the genes show a similar trend of expression change after treatment with the three compounds (Figs. 5 and S4). The similar trend of mRNA expression change of c-Myc target genes suggests that the three compounds can restrict the functionality of c-Myc resulting in the regulation of target genes' RNA. Till now, our study suggests that the compounds efficiently inhibit the functionality of c-Myc, which thereby results in apoptotic cell death.

CSCs are a rare population in the tumor mass with similar characteristics to the normal stem cells (48). The CSCs can differentiate in tumor cells and are highly resistant to available chemotherapy and radiotherapy (49). CSCs play a crucial role in cancer initiation and propagation and are identified as the root cause of cancer reoccurrence (50, 51). Recent studies have shown that targeting the CSC population has emerged as a preferred strategy to fully diminish the tumor volume for efficient cancer therapeutics (52, 53). c-Myc is a core CSC marker (54–56), and therefore, we explore the three compounds for their potential to restrict the growth and sphere-forming capacity of the CSCs. The rare CSC population was

isolated from the D341 cells using MACS. The three compounds showed appreciable antistemness properties, which were reflected from noteworthy cytotoxicity (Fig. 6*D*) and potent antisphere–forming potential (Fig. 6*E*) against CSCs.

The use of spectroscopic techniques has been proven efficient in studying the physical interaction of compounds with the macromolecules, especially proteins. Various biophysical experiments like fluorescence spectroscopy, fluorescence lifetime, and CD were employed to study the binding of the three compounds with the disordered c-Myc$_{910\text{-}960}$ peptide. The binding of compounds with c-Myc was initially determined by an equilibrium binding experiment employing fluorescence spectroscopy using the change in intrinsic fluorescence emission of Trp residue incorporated in the synthesized c-Myc$_{910\text{-}960}$ peptide. The indole moiety of Trp is very sensitive to changes in polarity around its environment. The ligand-binding at specific sites of proteins is often examined using the changes in fluorescence intensity of Trp residues, revealing the conformational changes in overall structure (57). A concentration-dependent quenching of the intrinsic Trp fluorescence was observed when the target disordered peptide was incubated with gradient concentrations of the compounds (Fig. 7*A*). The quenching of the Trp fluorescence was attributed to the change in c-Myc conformation in the presence of compounds. The Stern–Volmer plot describing the static or dynamic quenching of try intrinsic fluorescence by compounds is also depicted the in the Figure 7*A*. The downward deviation from the linearity is suggestive of the presence of two fluorophore populations out of which one remains inaccessible to the quencher. Accordingly, F0909-0360 is quenching most of the fluorescence from try residue then the reported inhibitor 10074-G5, followed by F0909-0073 and F1021-0686.

Time-resolved fluorescence of Trp residues in proteins has demonstrated the complexity of protein dynamics and thus is widely used to determine the interactions between proteins and ligands (58). A substantial decrease in the Trp fluorescence lifetime was also observed with the increasing concentration of the compounds (Fig. 7*B* and Table S6). The data from fluorescence spectroscopy and fluorescence lifetime indicate a change in the conformational dynamics of the disordered c-Myc due to the binding of the compounds. CD spectroscopy is a sensitive technique providing invaluable information about the proteins' conformations at the secondary level. The CD spectra in the far-UV region distinguish the different secondary structures of proteins (59); therefore, the conformational dynamics of c-Myc on binding with the studied compounds are analyzed using CD spectroscopy. The signature minimum at 200 nm indicated the random coil conformation of the free c-Myc peptide. A reduction in negative peak ellipticity at 200 nm of the c-Myc peptide was observed in the presence of the compounds (Fig. 7*C*). However, no characteristic negative peaks for α-helix or β-sheets were observed in the presence of the compounds, which indicates that the binding of compounds does not favor the formation of secondary structural elements. The comprehensive biophysical studies confirmed the change in c-Myc conformation in the presence of the compounds, suggesting the binding of the compounds to the disordered c-Myc; however, the c-Myc peptide remained disordered upon binding.

Till now, the data have suggested that the three compounds showed noticeable binding toward the disordered c-Myc, which results in the functional inhibition of the target protein leading to apoptotic cell death in cancer and CSCs. In the isolated form, c-Myc displays a partially folded conformation, and therefore, compounds showing stable binding with the target having a flexible backbone are of utmost importance. We employed 200 ns of extensive computational simulation with the three compounds in complex with both frames. The simulation parameters RMSD and RMSF showed less fluctuation, demonstrating a stable protein–ligand complex formation (Fig. S5). The stability of both the frame complexes is mainly attributed to the Glu957 residues, which were found to be interacting with all the residues throughout the simulation period. Additionally, the residue Glu957 is one of the identified hot spot that showed the maximum change in the binding free energy when mutated to the alanine residue. Based on the computational data, it can be inferred that Glu957 plays a crucial role in c-Myc/MAX heterodimerization, and its stable interactions with the compounds inhibit the formation of onco-dimer, leading to the functional repression of the c-Myc.

In the last few decades, several attempts have been made to discover novel inhibitor molecules that exclusively inhibit the functionality of c-Myc. Researchers have employed various transcriptional and posttranslational inhibition strategies, but for now, no inhibitor has gotten clinical approval. The three compounds, *i.e.,* F0909-0073, F0909-0360, and F1021-0686, reported from this study have shown confidence as a potential c-Myc inhibitor. The computational, *in vitro*, and biophysical studies have shown that these compounds have demonstrated an excellent potential to bind to the disordered bHLH domain of c-Myc, leading to its functional repression resulting in low micromolar to nanomolar IC$_{50}$ values against the c-Myc expressing cells. Several molecules have been reported as a functional inhibitor of c-Myc, but only a few like, 10058-F4, 10074-A4, 10074-G5, and KJ-Pyr-9, have been studied for their binding with the c-Myc peptide (21, 32, 60). Studies employing various biophysical techniques have shown that these reported inhibitor molecules physically interact with the c-Myc in the homogenous environment. Additionally, the CD studies have shown that the interaction of the compounds resulted in the decrease of the partially folded disordered structure of c-Myc without the formation of secondary structural elements, *i.e.*, α-helix or β-sheets, which was also observed in this study.

Targeting the disordered domain involved in PPI has always been a demanding task for clinical therapeutics. However, the identification and subsequent targeting of the hot spot residues have proven successful against the PPIs. Our study collectively reported the implication of hot spot targeting to discover novel inhibitor molecules *via* employing the conformation ensemble approach against disordered c-Myc. Furthermore, the study reported an excellent *in vitro* potency of the compounds achieved due to a stable interaction with the disordered target

c-Myc. The newly discovered compounds can be further preclinically tested for their pharmacokinetic and pharmacodynamic behavior and *in vivo* efficacy. Additionally, these three compounds can be further studied as lead molecules and functionally optimized to increase their overall efficacy.

Experimental procedures

Cell culture

The human HL-60, HT-29, U-87 MG, and HEK-293T were bought from National Centre for Cell Science. The human medulloblastoma cell line (D341) was procured from the American Type Culture Collection. The HL-60 cells were maintained in RPMI 1640 (Thermo Fisher Scientific), and the HT-29, U-87 MG, and HEK-293T cells were maintained in DMEM (Hyclone) medium supplemented with 10% fetal bovine serum (Sigma Aldrich), 1% antibiotic-anti-mycotic (Thermo Fisher Scientific), and 1% sodium pyruvate (Thermo Fisher Scientific). The D341 cells were maintained in Eagle's Minimum Essential Medium (BD Biosciences) media supplemented with 20% fetal bovine serum and 1% penicillin–streptomycin (Thermo Fisher Scientific). All the cells were grown in a humid environment at 37 °C with 5% CO2.

Disorder prediction

Several crystal and solution NMR structures of c-Myc are available in the Protein Data Bank with different binding partners, *i.e.,* protein and DNA. We have taken the crystal structure of c-Myc (chain A) in complex with MAX (chain B) protein (PDB ID: 1NKP (61)) for our study. We have utilized seven different predictors, namely, predictor of natural disordered regions VLXT, VSL2, VL3, FIT, IUPred2A Long and Short, and PrDos, to analyze the propensity of disorderness in the Myc protein sequence (from PDB ID: 1NKP; chain A). To reduce the prediction biasedness due to one predictor's value, we have calculated the mean values of each residue from each predictor with standard error. The cut-off value of each predictor is 0.5, the residues of ≥0.5 are considered to be disordered, and further, the percentage of predicted intrinsic disorder is calculated by dividing the number of residues ≥0.5 with the total number of Myc residues. The detailed methodology is given in our previously published literature (62).

Hot spot identification

The hot spots present in the c-Myc/MAX interface were analyzed using the previously described method (63). Briefly, the structure of the c-Myc–MAX complex was preprocessed and subjected to 40 ns molecular dynamics simulation using SANDER and particle mesh Ewald molecular dynamics modules of Amber 11 software suit http://ambermd.org/contributors, (Accessed June 7, 2021). Next, MM-PBSA method (64–66) was employed to evaluate the c-Myc–MAX complex total binding energy, per-residue energy, and alanine scanning mutagenesis energy. Subsequently, the c-Myc residues were classified as hot, warm, and null spots based on their energy difference between native and mutant protein complex.

Molecular dynamics simulations

The two chains were separated and prepared by adding missing hydrogens and correcting bond parameters and followed by optimization and energy minimization using OPLS 2005 forcefield in Schrodinger's *Protein preparation wizard* tool (67). Then, the prepared structure was placed in an orthorhombic simulation box with a distance of 10 Å from each edge of the box in the Desmond simulation package (68). The simulation system was then mixed with 0.15 M NaCl salt concentration for proper electrostatic distribution and charge neutralized by adding counterions. After building, the simulation setup was energy minimized using steepest descent and LBFGS methods for 2000 iterations, followed by equilibration using NPT ensemble till 1 ns. Lastly, the production MD run was executed for ∼410 ns using OPLS 2005 forcefield at an average temperature of 310K and pressure at 1 bar maintained by Berendsen thermostat and barostat algorithms. The hydrogen bonds were constrained using the LINear Constraint Solver algorithm (69). A similar procedure was followed for simulating protein–ligand complexes for 200 ns timescale each. For analyzing the simulation results, we have utilized simulation event analysis for RoG and energy parameters calculation and simulation interaction diagram tools of Desmond for RMSD and RMSF calculation. The visualization of simulation frames and binding conformations was done in Schrodinger's Maestro.

Conformational ensemble generation

From MD simulations of c-Myc structure up to ∼410 ns, over four lakh frames were generated and analyzed for further virtual screening. We have considered two variables (RMSD and RoG) against the potential energy of each frame in two separate calculations (*i.e.,* RMSD *versus* energy and RoG *versus* energy). Using these parameters, we have mapped the population of frames on 2D histogram plots for identifying conformations falling in similar energy and RMSD or RoG. Based on these two calculations, we have identified two frames [named as 'Frame 1 (F1)' and 'Frame 2 (F2)'] with calculated values (one from RMSD *versus* energy and one from RoG *versus* energy) for the virtual docking process.

Molecular docking

We have chosen PPI-focused libraries provided by Life Chemicals Inc, for virtual screening against the two identified conformations of c-Myc. A total of 29,517 ligands were processed through the *LigPrep* module (70) of Schrodinger for generating 3D conformations with stereoisomers and tautomeric states. After preparation, 54,143 conformations were produced for docking. As previously described in our published studies, we used Schrodinger's Glide scoring function for docking calculations (71). The docking was done against identified hot spot and warm spot residues in c-Myc. The center of grid coordinates for F1 are 1.4, -9.8, and 1.4 Å and F2 are 1.3, -10.1, and 1.9 Å. The three-step process for hit identification of Glide, *i.e.,* HTVS, SP, and XP, were employed. Then, the resultant hits were examined for binding energy

with c-Myc conformers using the *Prime* module, which employs MM-GBSA approach. Finally, the compounds based on docking score, binding energy, and interaction with hot spot and warm spot residues were screened manually for both the frames and selected for *in-vitro* validation.

In vitro *anticancer study*

For the anticancer studies, 5×10^3 cells were seeded in a 96-well plated and incubated with different concentrations of the compounds purchased from Life Chemicals. The cells were incubated for 48 h along with all experimental controls. For vehicle control, 0.2% dimethyl sulfoxide (DMSO) was used. After incubation, 10% MTT dye was added to each well and further incubated for 3 h. After adding DMSO, the absorbance was recorded in the Tecan Infinite M200 PRO plate reader at 570 nm with 650 nm as a reference. The cytotoxicity data were analyzed in GraphPad Prism 7, and the half-maximal inhibitory concentration, *i.e.,* IC50 value, was calculated by [inhibitor] *versus* response—variable slope (four parameters) in GraphPad Prism 7.

Real-time quantitative PCR and gene array

Two cell lines, *i.e.,* D341 and HL-60, were treated with different concentrations of F0909-0073, F0909-0360, and F1021-0686 for 36 h. Total RNA was isolated using the RNA-XPress reagent (HiMedia), considering the manufacturer's protocol. 1 μg RNA was used for cDNA synthesis using iScript Select cDNA synthesis kit (Bio-Rad), including the equal ratio (1:1) of both oligo(dT)20 and random primers. For real-time PCR, Hi-SYBr Master Mix (HiMedia) was used for reaction setup, and the fluorescence measurement was quantified in CFX96 Touch Real-Time PCR Detection System (Bio-Rad). The list of primers used in the study is summarized in Table S2. To study the change in expression of an array of c-Myc target genes, we analyzed the predesigned 384-well panel MYC Targets (SAB Target List) H384, Bio-Rad Laboratories. Total RNA (1 μg) was isolated from the HL-60 cells after treating the three compounds for 36 h. The RNA was reverse transcribed to cDNA using the iScript Select cDNA synthesis kit (Bio-Rad). RT-PCR was performed using two replicates for all the treatments employing the manufacturer protocol using three reference genes, glyceraldehyde-3-phosphate dehydrogenase, hypoxanthine phosphoribosyl transferase 1, and TATA box binding protein.

Western blot

D341 cells were treated with different concentrations of the three compounds, *i.e.,* F0909-0073, F0909-0360, and F1021-0686, for 36 h. The detailed protocol used for protein isolation and Western blot was adapted from our previous study (34). Briefly, RIPA buffer (25 mM Tris•HCl pH 7.6, 150 mM NaCl, 1% NP-40, 1% sodium deoxycholate, 0.1% SDS) along with Halt Protease Inhibitor Cocktail (Thermo Fisher Scientific) was used to prepare the cell lysate. After determining protein concentration, an equal volume of protein was electrophoresed using SDS-PAGE gels, and the bands were transferred to preactivated PVDF membranes (Merck Millipore). Next, the blots were probed with respective primary antibodies at 4 °C overnight, followed by incubation with horseradish peroxidase–conjugated secondary antibodies at room temperature. The blots were then developed with Clarity Western ECL Substrate and imaged in Amersham Imager 600 (GE), and the band intensity was quantified using ImageJ software. The list of antibodies used in the study is summarized in Table S1.

Annexin V/propidium iodide apoptosis assay

For apoptosis analysis, HT-29 cells were treated with different concentrations of F0909-0073, F0909-0360, and F1021-0686 for 24 h. For voltage and fluorescence compensation, single stain controls were used along with the negative control. The cells were then harvested and washed with PBS and incubated with Annexin V-Alexa Fluor 488 conjugate (Cat No. A13201, Thermo Fisher Scientific) and propidium iodide (Cat No. P3566, Thermo Fisher Scientific) for 30 min at RT. Ten thousand events per sample were collected in LSRFortessa cell analyzer, and the data acquisition and analysis were achieved using BD FACSDiva software.

Isolation and maintenance of CSCs

CSCs were isolated from the medulloblastoma cell line, D341, using MACS methods. Cell positive for CD133 surface markers were isolated from the D341 cell lines using CD133 MicroBeads (Miltenyi Biotec, Cat No: 130–100–857) following the manufacturer's protocol. Briefly, 10^7 D341 cells were incubated with FcR Blocking Reagent and CD133 MicroBeads for 20 min at 4 °C with continuous rotation. Next, cells were washed to remove the unbound beads and resuspended in wash buffer. The LC column was prepared by rinsing with the wash buffer in the presence of a magnetic field. The CD133+ cells were separated *via* passing the cell suspension through the magnetized LC column, which was collected by removing the column from the magnetic field. The CD133+ cells were then cultured in the low-attachment plates in serum-free culture media (DMEM/F12 with 20 ng/ml EGF, 20 ng/ml bFGF, B27 [without vitamin A], and penicillin-streptomycin). The isolated CSCs were characterized *via* qPCR and Western blot based on the expression of several CSCs markers like CD133, SOX2, Oct4, Nanog, and c-Myc.

In vitro *cytotoxicity on CSC*

3×10^3 D341-CSCs were seeded in a low-attachment U-shaped 96-well plate and incubated with different concentrations F0909-0073, F0909-0360, F1021-0686, and 10074-G5 with all experimental controls. The cells were incubated with the compounds for 48 h and further incubated with MTT for 2.5 h. The formazan crystals were dissolved with DMSO, and the absorbance was recorded at 570 nm with 650 nm as a reference in the Tecan Infinite M200 PRO plate reader.

Sphere formation assay

The tumorsphere of D341-CSCs was dissociated using Liberase TM (Roche, Cat. No. 5401119001), and the single-cell

suspension was obtained by passing the cell suspension through the 35 μm cell strainer. Then, 500 single cells were seeded in a low-attachment 12-well plate and treated with 10 μM of F0909-0073, F0909-0360, F1021-0686, and 10074-G5 for 7 days with the addition of fresh media after 4 days. After incubation, the spheres were counted on an inverted microscope, and the data were quantified using ImageJ software.

Steady-state fluorescence emission

For biophysical experiments, the c-Myc$_{910\text{-}960}$ peptide (90% purity) was purchased from Thermo Fisher Scientific. The sequence used for peptide synthesis was as follows: [NH2]-ERQRRNELKRSFFALRDQIPELENNEKAPKVVILKKATAWIL SVQAEEQKL-[COOH]. The intrinsic fluorescence of Trp residue of the c-Myc$_{910\text{-}960}$ peptide was measured using Horiba's Fluorolog-3 spectrofluorometer system from 310 nm to 500 nm wavelength range at 25 °C. The fluorescence measurements were performed in a 1 cm quartz cuvette where the excitation was kept at 295 nm, and the width of both excitation and emissions slits were set at 3 nm. c-Myc concentration was kept constant at 2 μM for all experiments while the concentration of all the investigated compounds (F1021-0686, F0909-0073, and F0909-0360) and the control compound (10074-G5) was varied from 0.01 μM to 1 μM to observe the effect on Trp fluorescence. The buffer system consisted of 20 mM sodium phosphate at physiological pH 7.4. The inner filter effect in the observed fluorescence, if any, was corrected as described by Lakowicz using the following equation (72):

$$F_{cor} = F_{obs} 10^{(Aex+Aem)/2}$$

Where, F_{cor} is the corrected fluorescence, F_{obs} is the observed fluorescence, and Aex and Aem are the absorbance values of the sample at excitation and emission wavelengths, respectively.

Fluorescence lifetime measurements

Fluorescence lifetime decay of Trp residue in c-Myc$_{910\text{-}960}$ peptide was obtained using the DeltaFlex T CSPC (Horiba Scientific Inc) system. The excitation was kept at 284 nm with a pulsed LED source, and the emission was recorded at 345 nm wavelength. Ludox was used to correct the instrument response factor at 284 nm. The concentration of c-Myc was kept constant at 7.5 μM for all the experiments. The lifetime decay of Trp was measured in the presence and absence of all three studied compounds as well as the control compound at different concentrations: 5 μM, 10 μM, 15 μM, 20 μM, and 25 μM. The buffer consisted of 20 mM sodium phosphate (pH 7.4) for every measurement. The resultant data were analyzed using the DAS6 software, and the lifetime values were calculated by fitting the data using a tri-exponential function having the best chi-square value approaching 1.0.

CD spectral measurements

The far-UV CD spectra corresponding to c-Myc$_{910\text{-}960}$ peptide were recorded using the J-1000 series JASCO spectrophotometer from 190 nm to 240 nm wavelength at 25 °C. The bandwidth was kept at 0.5 mm, and the path length of the quartz cuvette was 1 mm. The c-Myc CD scans were normalized using the buffer baselines composed of 20 mM sodium phosphate (pH 7.4). For binding experiments with compounds, CD spectra of c-Myc were normalized with CD baselines of individual compounds. The concentration of c-Myc was kept at 10 μM for all experiments.

Statistical analysis

For all the experiments, three technical/experimental replicates were studied until specified in the figure legends. The results are expressed as mean with either standard deviation or standard error mean, clearly mentioned in the figure legend. Significant differences were calculated using the Student's t test and analysis of variance in GraphPad Prism 7. Results with p-value < 0.05 were considered statistically significant.

Data availability

The data generated and supporting this manuscript's conclusion are included in the main text file and supporting information.

Supporting information—This article contains supporting information.

Acknowledgments—The BioX Centre and Advanced Materials Research Centre of the Indian Institute of Technology Mandi are highly acknowledged for providing experimental and HPC facilities. A. S. is thankful to the University Grants Commission, India, and T.B. is thankful to the Department of Science and Technology-INSPIRE, India, for the Doctoral research fellowship. R. G. is thankful to the Department of Science and Technology, India (BT/11/IYBA/2018/06).

Author contributions—A. S., R. G., and N. G. conceptualization; A. K., P. K., S. S., T. B., and N. N. methodology; A. S., P. K., S. S., T. B., N. N., M. S. C., R. G., and N. G. formal analysis; A. S., P. K., S. S., and T. B. writing-original draft; A. S., R. G., and N. G. writing-review and editing; R. G. and N. G. supervision; R. G. and N. G. funding acquisition.

Funding and additional information—N. G. acknowledges the Science and Engineering Research Board grant, India (ECR/2017/00092) and the seed grant under the Institute of Eminence Scheme, Banaras Hindu University for financial support.

Conflict of interest—The authors declare that they have no conflicts of interest with the contents of this article.

Abbreviations—The abbreviations used are: ASM, alanine scanning mutagenesis; bHLH-LZ, basic helix-loop-helix leucine-zipper; CD, circular dichroism; CSC, cancer stem cell; DMSO, dimethyl sulfoxide; HTVS, high-throughput virtual screening; IDP, intrinsically disordered protein; MACS, magnetic-activated cell sorting; MAX, Myc-associated factor X; MD, molecular dynamics; MM-GBSA, molecular mechanics generalized Born surface area; MM-PBSA, molecular mechanics Poisson–Boltzmann surface area; MTT, 3-(4,5-dimethylthiazol-2-yl)-2,5-diphenyltetrazolium bromide; PPI,

protein–protein interaction; RMSF, root mean square fluctuation; RoG, radius of gyration; SP, standard precision; Trp, tryptophan; XP, extra precision.

References

1. Jones, S., and Thornton, J. M. (1996) Principles of protein-protein interactions. *Proc. Natl. Acad. Sci. U. S. A.* **93**, 13–20
2. Nooren, I. M. A., and Thornton, J. M. (2003) Diversity of protein-protein interactions. *EMBO J.* **22**, 3486–3492
3. Deng, M., Zhang, K., Mehta, S., Chen, T., and Sun, F. (2003) Prediction of protein function using protein-protein interaction data. *J. Comput. Biol.* **10**, 947–960
4. Klein, M. A. (2014) Stabilized helical peptides: A strategy to target protein-protein interactions. *ACS Med. Chem. Lett.* **5**, 838–839
5. Stumpf, M. P. H., Thorne, T., De Silva, E., Stewart, R., Hyeong, J. A., Lappe, M., and Wiuf, C. (2008) Estimating the size of the human interactome. *Proc. Natl. Acad. Sci. U. S. A.* **105**, 6959–6964
6. Fry, D. C., and Vassilev, L. T. (2005) Targeting protein-protein interactions for cancer therapy. *J. Mol. Med.* **83**, 955–963
7. Harris, C. C. (2006) Protein-protein interactions for cancer therapy. *Proc. Natl. Acad. Sci. U. S. A.* **103**, 1629–1660
8. Moreira, I. S., Fernandes, P. A., and Ramos, M. J. (2007) Hot spots - a review of the protein-protein interface determinant amino-acid residues. *Proteins* **68**, 803–812
9. Clackson, T., and Wells, J. A. (1995) A hot spot of binding energy in a hormone-receptor interface. *Science* **267**, 383–386
10. Bogan, A. A., and Thorn, K. S. (1998) Anatomy of hot spots in protein interfaces. *J. Mol. Biol.* **280**, 1–9
11. Liu, Q., Chen, P., Wang, B., Zhang, J., and Li, J. (2018) Hot spot prediction in protein-protein interactions by an ensemble system. *BMC Syst. Biol.* **12**, 132
12. Keskin, O., Ma, B., and Nussinov, R. (2005) Hot regions in protein-protein interactions: The organization and contribution of structurally conserved hot spot residues. *J. Mol. Biol.* **345**, 1281–1294
13. Dang, C. V. (2012) MYC on the path to cancer. *Cell* **149**, 22–35
14. Amati, B., Frank, S. R., Donjerkovic, D., and Taubert, S. (2001) Function of the c-Myc oncoprotein in chromatin remodeling and transcription. *Biochim. Biophys. Acta* **1471**, M135–M145
15. Rahl, P. B., and Young, R. A. (2014) MYC and transcription elongation. *Cold Spring Harb. Perspect. Med.* **4**, a020990
16. Dang, C. V., O'Donnell, K. A., Zeller, K. I., Nguyen, T., Osthus, R. C., and Li, F. (2006) The c-Myc target gene network. *Semin. Cancer Biol.* **16**, 253–264
17. Carabet, L., Rennie, P., and Cherkasov, A. (2018) Therapeutic inhibition of Myc in cancer. Structural bases and computer-aided drug discovery approaches. *Int. J. Mol. Sci.* **20**, 120
18. Kalkat, M., De Melo, J., Hickman, K., Lourenco, C., Redel, C., Resetca, D., Tamachi, A., Tu, W., and Penn, L. (2017) MYC deregulation in primary human cancers. *Genes (Basel)* **8**, 151
19. Coudé, M. M., Braun, T., Berrou, J., Dupont, M., Bertrand, S., Masse, A., Raffoux, E., Itzykson, R., Delord, M., Riveiro, M. E., Herait, P., Baruchel, A., Dombret, H., and Gardin, C. (2015) BET inhibitor OTX015 targets BRD2 and BRD4 and decreases c-MYC in acute leukemia cells. *Oncotarget* **6**, 17698–17712
20. Handoko, L., Kaczkowski, B., Hon, C. C., Lizio, M., Wakamori, M., Matsuda, T., Ito, T., Jeyamohan, P., Sato, Y., Sakamoto, K., Yokoyama, S., Kimura, H., Minoda, A., and Umehara, T. (2018) JQ1 affects BRD2-dependent and independent transcription regulation without disrupting H4-hyperacetylated chromatin states. *Epigenetics* **13**, 410–431
21. Hart, J. R., Garner, A. L., Yu, J., Ito, Y., Sun, M., Ueno, L., Rhee, J. K., Baksh, M. M., Stefan, E., Hartl, M., Bister, K., Vogt, P. K., and Janda, K. D. (2014) Inhibitor of MYC identified in a Kröhnke pyridine library. *Proc. Natl. Acad. Sci. U. S. A.* **111**, 12556–12561
22. Fletcher, S., and Prochownik, E. V. (2015) Small-molecule inhibitors of the Myc oncoprotein. *Biochim. Biophys. Acta* **1849**, 525–543
23. Li, B., and Simon, M. C. (2013) Molecular pathways: Targeting MYC-induced metabolic reprogramming and oncogenic stress in cancer. *Clin. Cancer Res.* **19**, 5835–5841
24. Conacci-Sorrell, M., McFerrin, L., and Eisenman, R. N. (2014) An overview of MYC and its interactome. *Cold Spring Harb. Perspect. Med.* **4**, a014357
25. Jin, F., Yu, C., Lai, L., and Liu, Z. (2013) Ligand clouds around protein clouds: A scenario of ligand binding with intrinsically disordered proteins. *PLoS Comput. Biol.* **9**, e1003249
26. Uversky, V. N. (2011) Intrinsically disordered proteins from A to Z. *Int. J. Biochem. Cell Biol.* **43**, 1090–1103
27. Tompa, P. (2011) Unstructural biology coming of age. *Curr. Opin. Struct. Biol.* **21**, 419–425
28. Oldfield, C. J., and Dunker, A. K. (2014) Intrinsically disordered proteins and intrinsically disordered protein regions. *Annu. Rev. Biochem.* **83**, 553–584
29. Dunker, A. K., and Uversky, V. N. (2010) Drugs for "protein clouds": Targeting intrinsically disordered transcription factors. *Curr. Opin. Pharmacol.* **10**, 782–788
30. Cheng, Y., LeGall, T., Oldfield, C. J., Mueller, J. P., Van, Y. Y. J., Romero, P., Cortese, M. S., Uversky, V. N., and Dunker, A. K. (2006) Rational drug design *via* intrinsically disordered protein. *Trends Biotechnol.* **24**, 435–442
31. Metallo, S. J. (2010) Intrinsically disordered proteins are potential drug targets. *Curr. Opin. Chem. Biol.* **14**, 481–488
32. Follis, A. V., Hammoudeh, D. I., Wang, H., Prochownik, E. V., and Metallo, S. J. (2008) Structural rationale for the coupled binding and unfolding of the c-Myc oncoprotein by small molecules. *Chem. Biol.* **15**, 1149–1155
33. Uversky, V. N. (2012) Intrinsically disordered proteins and novel strategies for drug discovery. *Expert Opin. Drug Discov.* **7**, 475–488
34. Singh, A., Kumar, A., Kumar, P., Nayak, N., Bhardwaj, T., Giri, R., and Garg, N. (2021) A novel inhibitor L755507 efficiently blocks c-Myc–MAX heterodimerization and induces apoptosis in cancer cells. *J. Biol. Chem.* **297**, 100903
35. Dang, C. V. (1999) c-Myc target genes involved in cell growth, apoptosis, and metabolism. *Mol. Cell Biol.* **19**, 1–11
36. Choi, S. H., Mahankali, M., Lee, S. J., Hull, M., Petrassi, H. M., Chatterjee, A. K., Schultz, P. G., Jones, K. A., and Shen, W. (2017) Targeted disruption of Myc-max oncoprotein complex by a small molecule. *ACS Chem. Biol.* **12**, 2715–2719
37. Blundell, T. L., Burke, D. F., Chirgadze, D., Dhanaraj, V., Hyvonen, M., Axel Innis, C., Parisini, E., Pellegrini, L., Sayed, M., and Sibanda, B. L. (2000) Protein-protein interactions in receptor activation and intracellular signalling. *Biol. Chem.* **381**, 955–959
38. Conte, L. Lo, Chothia, C., and Janin, J. (1999) The atomic structure of protein-protein recognition sites. *J. Mol. Biol.* **285**, 2177–2198
39. Kim, D. E., Chivian, D., and Baker, D. (2004) Protein structure prediction and analysis using the Robetta server. *Nucleic Acids Res.* **32**, W526–W531
40. Darnell, S. J., LeGault, L., and Mitchell, J. C. (2008) KFC server: Interactive forecasting of protein interaction hot spots. *Nucleic Acids Res.* **36**, 265–269
41. Martins, S. A., Perez, M. A. S., Moreira, I. S., Sousa, S. F., Ramos, M. J., and Fernandes, P. A. (2013) Computational alanine scanning mutagenesis: MM-PBSA vs TI. *J. Chem. Theory Comput.* **9**, 1311–1319
42. Ibarra, A. A., Bartlett, G. J., Hegedüs, Z., Dutt, S., Hobor, F., Horner, K. A., Hetherington, K., Spence, K., Nelson, A., Edwards, T. A., Woolfson, D. N., Sessions, R. B., and Wilson, A. J. (2019) Predicting and experimentally validating hot-spot residues at protein-protein interfaces. *ACS Chem. Biol.* **14**, 2252–2263
43. Yu, B., Huang, Z., Zhang, M., Dillard, D. R., and Ji, H. (2013) Rational design of small-molecule inhibitors for β-catenin/T-cell factor protein–protein interactions by bioisostere replacement. *ACS Chem. Biol.* **8**, 524–529
44. Lise, S., Archambeau, C., Pontil, M., and Jones, D. T. (2009) Prediction of hot spot residues at protein-protein interfaces by combining machine learning and energy-based methods. *BMC Bioinformatics* **10**, 365

45. Uversky, V. N. (2013) Intrinsically disordered proteins. In *Brenner's Encyclopedia of Genetics*, Second Edition, Elsevier Inc, Amsterdam: 124–126
46. Amaro, R. E., Baudry, J., Chodera, J., Demir, Ö., McCammon, J. A., Miao, Y., and Smith, J. C. (2018) Ensemble docking in drug discovery. *Biophys. J.* **114**, 2271–2278
47. Evangelista Falcon, W., Ellingson, S. R., Smith, J. C., and Baudry, J. (2019) Ensemble docking in drug discovery: How many protein configurations from molecular dynamics simulations are needed to reproduce known ligand binding? *J. Phys. Chem. B.* **123**, 5189–5195
48. Yu, Z., Pestell, T. G., Lisanti, M. P., and Pestell, R. G. (2012) Cancer stem cells. *Int. J. Biochem. Cell Biol.* **44**, 2144–2151
49. Zhao, J. (2016) Cancer stem cells and chemoresistance: The smartest survives the raid. *Pharmacol. Ther.* **160**, 145–158
50. Manoranjan, B., Venugopal, C., McFarlane, N., Doble, B. W., Dunn, S. E., Scheinemann, K., and Singh, S. K. (2012) Medulloblastoma stem cells: Where development and cancer cross pathways. *Pediatr. Res.* **71**, 516–522
51. Singh, S. K., Hawkins, C., Clarke, I. D., Squire, J. A., Bayani, J., Hide, T., Henkelman, R. M., Cusimano, M. D., and Dirks, P. B. (2004) Identification of human brain tumour initiating cells. *Nature* **432**, 396–401
52. Shibata, M., and Hoque, M. O. (2019) Targeting cancer stem cells: A strategy for effective eradication of cancer. *Cancers (Basel)* **11**, 732
53. Sun, H. R., Wang, S., Yan, S. C., Zhang, Y., Nelson, P. J., Jia, H. L., Qin, L. X., and Dong, Q. Z. (2019) Therapeutic strategies targeting cancer stem cells and their microenvironment. *Front. Oncol.* **9**, 1104
54. Zhang, H. Le, Wang, P., Lu, M. Z., Zhang, S. D., and Zheng, L. (2019) c-Myc maintains the self-renewal and chemoresistance properties of colon cancer stem cells. *Oncol. Lett.* **17**, 4487–4493
55. Kim, W. T., and Ryu, C. J. (2017) Cancer stem cell surface markers on normal stem cells. *BMB Rep.* **50**, 285–298
56. Walcher, L., Kistenmacher, A. K., Suo, H., Kitte, R., Dluczek, S., Strauß, A., Blaudszun, A. R., Yevsa, T., Fricke, S., and Kossatz-Boehlert, U. (2020) Cancer stem cells—origins and biomarkers: Perspectives for targeted personalized therapies. *Front. Immunol.* **11**, 1280
57. Balaei, F., and Ghobadi, S. (2019) Hydrochlorothiazide binding to human serum albumin induces some compactness in the molecular structure of the protein: A multi-spectroscopic and computational study. *J. Pharm. Biomed. Anal.* **162**, 1–8
58. Li, M., and Hagerman, A. E. (2014) Role of the flavan-3-ol and galloyl moieties in the interaction of (-)-epigallocatechin gallate with serum albumin. *J. Agric. Food Chem.* **62**, 3768–3775
59. Greenfield, N. J. (2007) Using circular dichroism spectra to estimate protein secondary structure. *Nat. Protoc.* **1**, 2876–2890
60. Hammoudeh, D. I., Follis, A. V., Prochownik, E. V., and Metallo, S. J. (2009) Multiple independent binding sites for small-molecule inhibitors on the oncoprotein c-Myc. *J. Am. Chem. Soc.* **131**, 7390–7401
61. Nair, S. K., and Burley, S. K. (2003) X-ray structures of Myc-Max and Mad-Max recognizing DNA: Molecular bases of regulation by proto-oncogenic transcription factors. *Cell* **112**, 193–205
62. Giri, R., Bhardwaj, T., Shegane, M., Gehi, B. R., Kumar, P., Gadhave, K., Oldfield, C. J., and Uversky, V. N. (2021) Understanding COVID-19 *via* comparative analysis of dark proteomes of SARS-CoV-2, human SARS and bat SARS-like coronaviruses. *Cell Mol. Life Sci.* **78**, 1655–1688
63. Sarvagalla, S., Cheung, C. H. A., Tsai, J.-Y., Hsieh, H. P., and Coumar, M. S. (2016) Disruption of protein–protein interactions: Hot spot detection, structure-based virtual screening and *in vitro* testing for the anti-cancer drug target – survivin. *RSC Adv.* **6**, 31947–31959
64. Rastelli, G., Del Rio, A., Degliesposti, G., and Sgobba, M. (2010) Fast and accurate predictions of binding free energies using MM-PBSA and MM-GBSA. *J. Comput. Chem.* **31**, 797–810
65. Kollman, P. A., Massova, I., Reyes, C., Kuhn, B., Huo, S., Chong, L., Lee, M., Lee, T., Duan, Y., Wang, W., Donini, O., Cieplak, P., Srinivasan, J., Case, D. A., and Cheatham, T. E. (2000) Calculating structures and free energies of complex molecules: Combining molecular mechanics and continuum models. *Acc. Chem. Res.* **33**, 889–897
66. Hou, T., Wang, J., Li, Y., and Wang, W. (2011) Assessing the performance of the MM/PBSA and MM/GBSA methods. 1. The accuracy of binding free energy calculations based on molecular dynamics simulations. *J. Chem. Inf. Model.* **51**, 69–82
67. Madhavi Sastry, G., Adzhigirey, M., Day, T., Annabhimoju, R., and Sherman, W. (2013) Protein and ligand preparation: Parameters, protocols, and influence on virtual screening enrichments. *J. Comput. Aided. Mol. Des.* **27**, 221–234
68. Bowers, K. J., Chow, D. E., Xu, H., Dror, R. O., Eastwood, M. P., Gregersen, B. A., Klepeis, J. L., Kolossvary, I., Moraes, M. A., Sacerdoti, F. D., Salmon, J. K., Shan, Y., and Shaw, D. E. (2007) *Scalable Algorithms for Molecular Dynamics Simulations on Commodity Clusters*, Institute of Electrical and Electronics Engineers (IEEE), 43–43
69. Hess, Berk., Bekker, Henk., Berendsen Herman, J. C., and Fraaije Johannes, G. E. M. (1998) Lincs: A linear constraint solver for molecular simulations. *J. Comput. Chem.* **18**, 1463–1472
70. Greenwood, J. R., Calkins, D., Sullivan, A. P., and Shelley, J. C. (2010) Towards the comprehensive, rapid, and accurate prediction of the favorable tautomeric states of drug-like molecules in aqueous solution. *J. Comput. Aided. Mol. Des.* **24**, 591–604
71. Singh, A., Patel, S. K., Kumar, P., Das, K. C., Verma, D., Sharma, R., Tripathi, T., Giri, R., Martins, N., and Garg, N. (2020) Quercetin acts as a P-gp modulator *via* impeding signal transduction from nucleotide-binding domain to transmembrane domain. *J. Biomol. Struct. Dyn.* https://doi.org/10.1080/07391102.2020.1858966
72. Lakowicz, J. R. (2006) *Principles of Fluorescence Spectroscopy*, Springer Nature Switzerland, Cham